

Mutations in *KATNB1* Cause Complex Cerebral Malformations by Disrupting Asymmetrically Dividing Neural Progenitors

Ketu Mishra-Gorur,^{1,2,3,4,19} Ahmet Okay Çağlayan,^{1,2,3,4,19} Ashleigh E. Schaffer,⁵ Chiswili Chabu,^{2,6} Octavian Henegariu,^{1,2,3,4} Fernando Vonhoff,⁷ Gözde Tuğçe Akgümüş,^{1,2,3,4} Sayoko Nishimura,^{1,4} Wenqi Han,^{3,8} Shu Tu,⁹ Burçin Baran,^{1,2,3,4} Hakan Gümüş,¹⁰ Cengiz Dilber,¹¹ Maha S. Zaki,¹² Heba A.A. Hossni,¹³ Jean-Baptiste Rivière,¹⁴ Hülya Kayserili,¹⁵ Emily G. Spencer,⁵ Rasim Ö. Rosti,⁵ Jana Schroth,⁵ Hüseyin Per,¹⁰ Caner Çağlar,^{1,2,3,4} Çağrı Çağlar,^{1,2,3,4} Duygu Dölen,^{1,2,3,4} Jacob F. Baranoski,^{1,2,3,4} Sefer Kumandaş,¹⁰ Frank J. Minja,¹⁶ E. Zeynep Erson-Omay,^{1,2,3,4} Shrikant M. Mane,^{2,17} Richard P. Lifton,^{2,6} Tian Xu,^{2,6} Haig Keshishian,⁷ William B. Dobyns,¹⁸ Neil C. Chi,⁹ Nenad Sestan,^{3,4,8} Angeliki Louvi,^{1,3,4} Kaya Bilgüvar,^{2,17} Katsuhito Yasuno,^{1,2,3,4} Joseph G. Gleeson,^{5,*} and Murat Günel^{1,2,3,4,*}

¹Department of Neurosurgery

²Department of Genetics

³Department of Neurobiology

⁴Yale Program on Neurogenetics

Yale School of Medicine, New Haven, CT 06510, USA

⁵Neurogenetics Laboratory, Department of Neurosciences, Howard Hughes Medical Institute, University of California, San Diego, La Jolla, CA 92093, USA

⁶Howard Hughes Medical Institute, Yale School of Medicine, New Haven, CT 06510, USA

⁷Department of Molecular, Cellular and Developmental Biology, Yale University, New Haven, CT 06511, USA

⁸Kavli Institute for Neuroscience, Yale School of Medicine, New Haven, CT 06510, USA

⁹Department of Medicine, University of California, San Diego, La Jolla, CA 92093, USA

¹⁰Division of Pediatric Neurology, Department of Pediatrics, Erciyes University Medical Faculty, Kayseri 38039, Turkey

¹¹Division of Pediatric Neurology, Department of Pediatrics, Sütcü Imam University Medical Faculty, Kahramanmaraş 46100, Turkey

¹²Clinical Genetics Department, Human Genetics and Genome Research Division, National Research Center, Cairo 12311, Egypt

¹³Department of Neurology, National Institute of Neuromotor System, Cairo 12311, Egypt

¹⁴Equipe Génétique des Anomalies du Développement, EA 4271, Université de Bourgogne, 21078 Dijon, France

¹⁵Department of Medical Genetics, Istanbul Medical Faculty, Istanbul University, Istanbul 34093, Turkey

¹⁶Department of Radiology

¹⁷Yale Center for Genome Analysis

Yale School of Medicine, New Haven, CT 06510, USA

¹⁸Departments of Pediatrics and Neurology, University of Washington and Center for Integrative Brain Research, Seattle Children's Research Institute, Seattle, Washington 98105, USA

¹⁹Co-first author

*Correspondence: jogleeson@rockefeller.edu (J.G.G.), murat.gunel@yale.edu (M.G.)

<http://dx.doi.org/10.1016/j.neuron.2014.12.014>

SUMMARY

Exome sequencing analysis of over 2,000 children with complex malformations of cortical development identified five independent (four homozygous and one compound heterozygous) deleterious mutations in *KATNB1*, encoding the regulatory subunit of the microtubule-severing enzyme Katanin. Mitotic spindle formation is defective in patient-derived fibroblasts, a consequence of disrupted interactions of mutant *KATNB1* with *KATNA1*, the catalytic subunit of Katanin, and other microtubule-associated proteins. Loss of *KATNB1* orthologs in zebrafish (*katnb1*) and flies (*kat80*) results in microcephaly, recapitulating the human phenotype. In the developing *Drosophila* optic lobe, *kat80* loss specifically affects the asymmetrically dividing neuroblasts, which display supernumerary

centrosomes and spindle abnormalities during mitosis, leading to cell cycle progression delays and reduced cell numbers. Furthermore, *kat80* depletion results in dendritic arborization defects in sensory and motor neurons, affecting neural architecture. Taken together, we provide insight into the mechanisms by which *KATNB1* mutations cause human cerebral cortical malformations, demonstrating its fundamental role during brain development.

INTRODUCTION

A mechanistic understanding of human brain development has only recently begun to be elaborated at the gene level, with the discovery of disease-causing mutations in monogenic forms of malformations of cerebral cortical development (MCDs). MCD syndromes have traditionally been classified on the basis of

imaging findings that correlate with disturbances at distinct phases of cortical development, including proliferation of neural progenitors (e.g., leading to genetic forms of microcephaly), neuronal migration (e.g., pachygyria, lissencephaly, subcortical and periventricular heterotopias), and postmigrational development and organization (e.g., schizencephaly, polymicrogyria) (Barkovich et al., 2012). Phenotypic overlap between these MCD disorders is commonly observed, with a single gene mutation leading to multiple cortical abnormalities, suggesting that diverse cerebral malformations can have a unified underlying causation (Bilgüvar et al., 2010).

Genetic studies have also highlighted significant heterogeneity in the molecular pathways underlying MCDs, with the possible exception of autosomal recessive primary microcephaly (MCPH), which is associated with a plethora of genes (e.g., *ASPM*, *CDK5RAP2*, *CASC5*, *CENPJ*, *CEP63*, *CEP135*, *CEP152*, *STIL*, and *WDR62*) that encode proteins involved in cytoskeletal control of the mitotic apparatus, including centrosomes and mitotic spindle poles (Bettencourt-Dias et al., 2011; Bilgüvar et al., 2010; Kaindl et al., 2010; Thornton and Woods, 2009).

Despite dramatic differences in brain size and complexity, animal models have proven invaluable in elucidating the biology of MCDs, for example, by confirming the importance of centrosome in microcephaly (Kaindl et al., 2010). In *Drosophila*, homozygous loss of either *asp* (*abnormal spindle*, ortholog of human *ASPM*, mutated in MCPH5, OMIM#608716) or *cnn* (*centrosomin*, ortholog of human *CDK5RAP2*, mutated in MCPH3, OMIM#604804) affects asymmetric cell division during development (Bond et al., 2005; Wakefield et al., 2001). Similarly, both mouse and zebrafish models of human *SCL/TAL1-interrupting locus* gene (*STIL*), mutated in MCPH7 (OMIM#612703), have shown that *STIL* plays a role in centrosome duplication and function and mitotic spindle organization and signaling (Izraeli et al., 1999; Pfaff et al., 2007).

The centrosome functions as the primary microtubule-organizing center of the cell, and in humans, mutations in microtubule-associated proteins (DCX, LIS1, NDE1) (Alkuraya et al., 2011; Bakircioglu et al., 2011; Gleeson et al., 1998; Reiner et al., 1993) or tubulin isoforms (TUBA1A, TUBA8, TUBB2B, and TUBB3) (Abdollahi et al., 2009; Jaglin et al., 2009; Kumar et al., 2010; Tischfield et al., 2010) also underlie defects in cellular proliferation, neuronal migration, and cortical organization. Proper functioning of microtubules is in turn dependent on the tight control of their length, number, as well as cargo movement (Shu et al., 2004; Tanaka et al., 2004).

A concerted action of polymerizing and severing enzymes regulates microtubule length. Indeed, mutations in *SPAST*, encoding the microtubule-severing enzyme spastin, result in progressive axonal degeneration and autosomal dominant spastic paraplegia (SPG4, OMIM#182601), thus linking microtubule remodeling to neurodegeneration (Hazan et al., 1999). Katanin, the only other well-characterized microtubule-severing enzyme, composed of a catalytic, p60 (KATNA1), and a regulatory, p80 (KATNB1), subunit, acts by disrupting contacts within the polymer lattice (McNally and Vale, 1993). In developing neurons, Katanin localizes to microtubules and centrosomes and is essential for microtubule shortening and release (Ahmad et al., 1999). Katanin functions in cell division (McNally et al., 2006; Zhang et al., 2007), neuronal morphogenesis (Karabay et al., 2004; Yu et al.,

2008), and assembly and disassembly of cilia and flagella (Casanova et al., 2009; Sharma et al., 2007).

p60/KATNA1 is a member of the AAA (ATPases Associated with diverse cellular Activities) domain containing protein family, whereas p80/KATNB1 binds to p60 and targets it to subcellular structures including the centrosome, further mediating its interactions with Dynein, LIS1, and NDEL1 (Hartman et al., 1998; McNally et al., 2000). A missense mutation in the highly conserved WD40 domain of *Katnb1* has been shown to cause azoospermia and male sterility in mice (O'Donnell et al., 2012).

Here, by studying patients with MCDs, we identify deleterious mutations in *KATNB1* that result in a spectrum of MCD disorders, including microcephaly co-occurring with lissencephaly or less severe neuronal migration abnormalities such as periventricular or subcortical heterotopias. Knockdown of *KATNB1* orthologs in zebrafish (*Danio rerio*; *katnb1*) and *Drosophila* (*kat80*) results in a small brain, recapitulating the human phenotype. Further, in *Drosophila*, *kat80* is essential for the formation of the mitotic spindle, and its loss results in supernumerary centrosomes and delayed anaphase onset (AO), preferentially affecting asymmetrically dividing neuroblasts (NBs) in vivo. Lastly, *kat80* predominantly regulates neuronal dendritic arborization. Taken together, these findings demonstrate a fundamental role of *KATNB1* in human cerebral cortical development and pathology.

RESULTS

Whole-Exome Sequencing Identifies Recessive Mutations in *KATNB1* in Patients with Malformations of Cortical Development

We performed whole-exome capture and next-generation sequencing of germline DNA of over 2,000 children, who were mainly products of consanguineous unions. In Family 1 (NG-961), the two affected siblings (kinship coefficient 0.23; Table S1) displayed cognitive delay and seizures (Table S1). Physical exam revealed microcephaly, with MRI demonstrating subcortical heterotopia (Figure 1A; Table S1 available online). Exome-sequencing (Table S1) identified two homozygous predicted deleterious missense variants; one was previously reported and affected the *glucosaminyl (N-acetyl) transferase 2* gene (encoding a blood group II antigen) (p.Glu298Lys, rs139794913) resulting in cataracts, a phenotype not seen in our patients. The other, a p.Ser535Leu mutation, was novel and affected the *KATNB1* gene (Table S1).

Family 2 (NG-LIS-711), with a history of three early-pregnancy losses, also had two affected members (kinship coefficient of 0.12; Table S1) that exhibited severe cognitive delay and autistic features (Table S1). MRI scans confirmed microcephaly and revealed severe simplified gyral pattern and corpus callosum abnormality (Figure 1B; Table S1). Exome sequencing (Table S1) detected only two homozygous variants, one affected the *metallothionein-4* gene (p.TyrTrp300CysArg), while the other was a *KATNB1* predicted deleterious missense mutation (p.Leu540Arg) (Table S1).

In Family 3, a 21-month-old female (NG-MIC-2584) (who also had a sister that died 25 days after birth) presented to medical attention with jaundice, respiratory distress, and severe delay in motor and mental development and was found to be

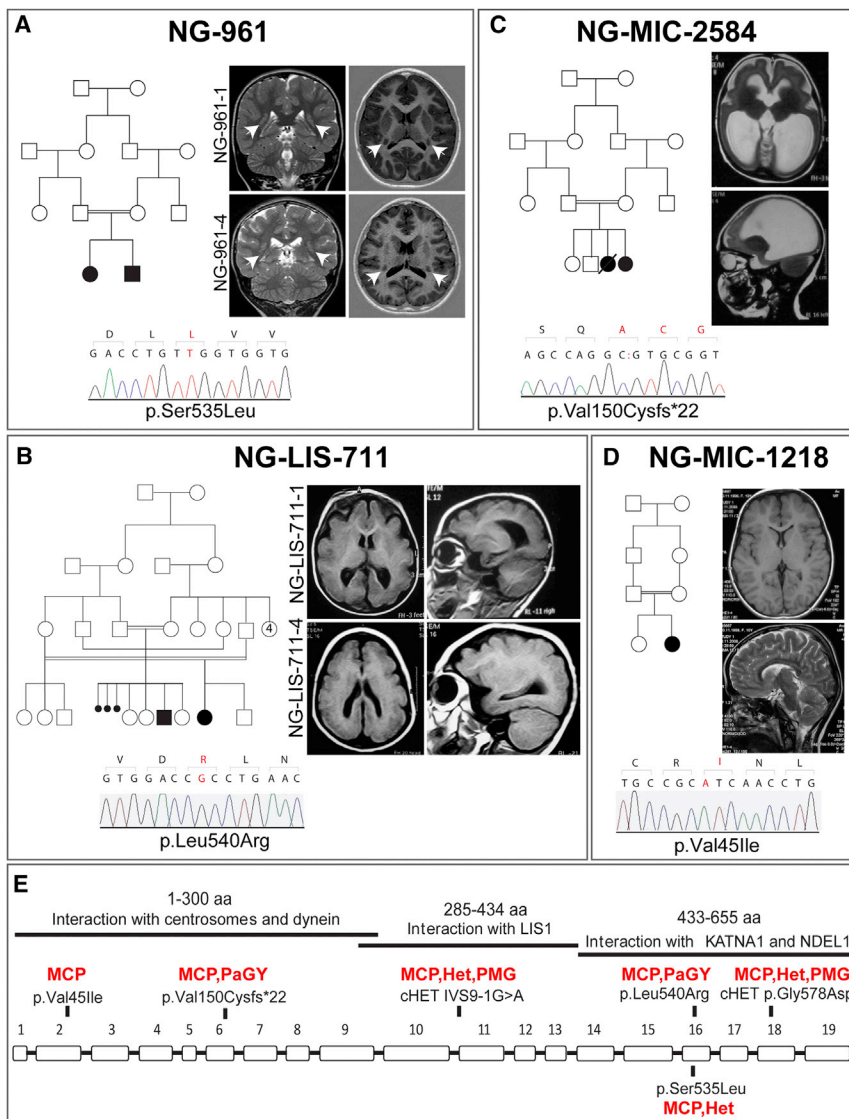


Figure 1. *KATNB1* Mutations in MCD Patients

(A) Kindred NG-961. Pedigree structure depicting a first cousin consanguineous union is shown on the left. Coronal T2-weighted images (left) and axial T1-weighted images (right) show symmetric nodular gray matter heterotopia in the bilateral corona radiata, indicated with white arrows, in both affected siblings. Sanger sequencing confirmation of the p.Ser535Leu mutation in *KATNB1* is shown at the bottom.

(B) Kindred NG-LIS-711. Complex pedigree structure is shown at left. Axial (left) and sagittal (right) T1-weighted images show diffuse pachygyria. A chromatogram of Sanger sequencing result, which confirmed the *KATNB1* p.Leu540Arg homozygous mutation in both affected children, is shown at the bottom.

(C) Kindred NG-MIC-2584. Pedigree structure demonstrating a first cousin consanguineous union with two affected children (one deceased) is shown on the left. Axial (upper) and sagittal (lower) T2-weighted images reveal a microlissencephalic brain with grossly dilated ventricles. Sanger sequencing confirmation of the p.Val150Cysfs*22 homozygous mutation is shown at the bottom.

(D) Kindred NG-MIC-1218. Pedigree structure (top left) and axial T1- (upper) and sagittal T2- (lower) weighted images revealing a microcephalic brain with grossly normal architecture. The patient is homozygous for the p.Val45Ile mutation (bottom).

(E) Exon-intron structure of *KATNB1* is shown. Solid bars on top indicate the functional interaction domains and their localization to the *KATNB1* protein. The location of each mutation and the associated phenotype are noted. MCP, microcephaly; Het, heterotopia; PaGY, pachygyria; PMG, polymicrogyria (see also Figure S1; Table S1).

microcephalic (Table S1). MRI demonstrated microlissencephaly and grossly dilated ventricles (Figure 1C). Exome sequencing revealed a homozygous frameshift mutation (p.Val150Cysfs*22) in *KATNB1*.

In Family 4, the patient (NG-MIC-1218-4) exhibited mild cognitive delay (Table S1). Her MRI was mainly remarkable for microcephaly (Figure 1D). Exome sequencing of the patient and her unaffected sibling (kinship coefficient of 0.23; Table S1) identified 21 homozygous variants observed only in the patient. Twelve of these variants were novel, including a predicted deleterious missense mutation (p.Val45Ile) in *KATNB1*.

Prompted by the identification of multiple independent homozygous mutations in *KATNB1*, we then searched our exome sequencing databases for any potential compound heterozygous patients and identified a fifth patient (NG-PNH 226). This was a single affected offspring of a nonconsanguineous union whose clinical and radiologic findings have previously been reported (Wieck et al., 2005). She displayed severe cognitive and

motor developmental delay and advanced microcephaly; MRI confirmed the microcephaly and revealed partial genesis of corpus callosum, polymicrogyria, and posterior predominant periventricular nodular heterotopia (Table S1). Analysis of her exome sequencing results did not identify any homozygous variants in the known MCD genes, but revealed two heterozygous *KATNB1* mutations: a splice acceptor (IVS9-1G > A; g.57787300G > A) variant and a predicted deleterious missense mutation (p.Gly578Asp; g.57790282G > A) (Figure 1E; Table S1). Sanger sequencing proved the patient to be compound heterozygous for the *KATNB1* mutations with each of the variants being inherited from one of the parents (Figure S1).

To summarize, brain imaging of *KATNB1* mutant patients demonstrated severe microcephaly with diffuse frontal predominant undersulcation (only the frontal lobe in NG-MIC-1218) with variable gyral size, mildly thick cortex with subtle irregularity of the cortical-white matter border, but no clear microgyri, variable subcortical or periventricular heterotopia, variable hypogenesis of the corpus callosum, and relatively preserved brainstem and cerebellum. The cortical malformation thus differs from both

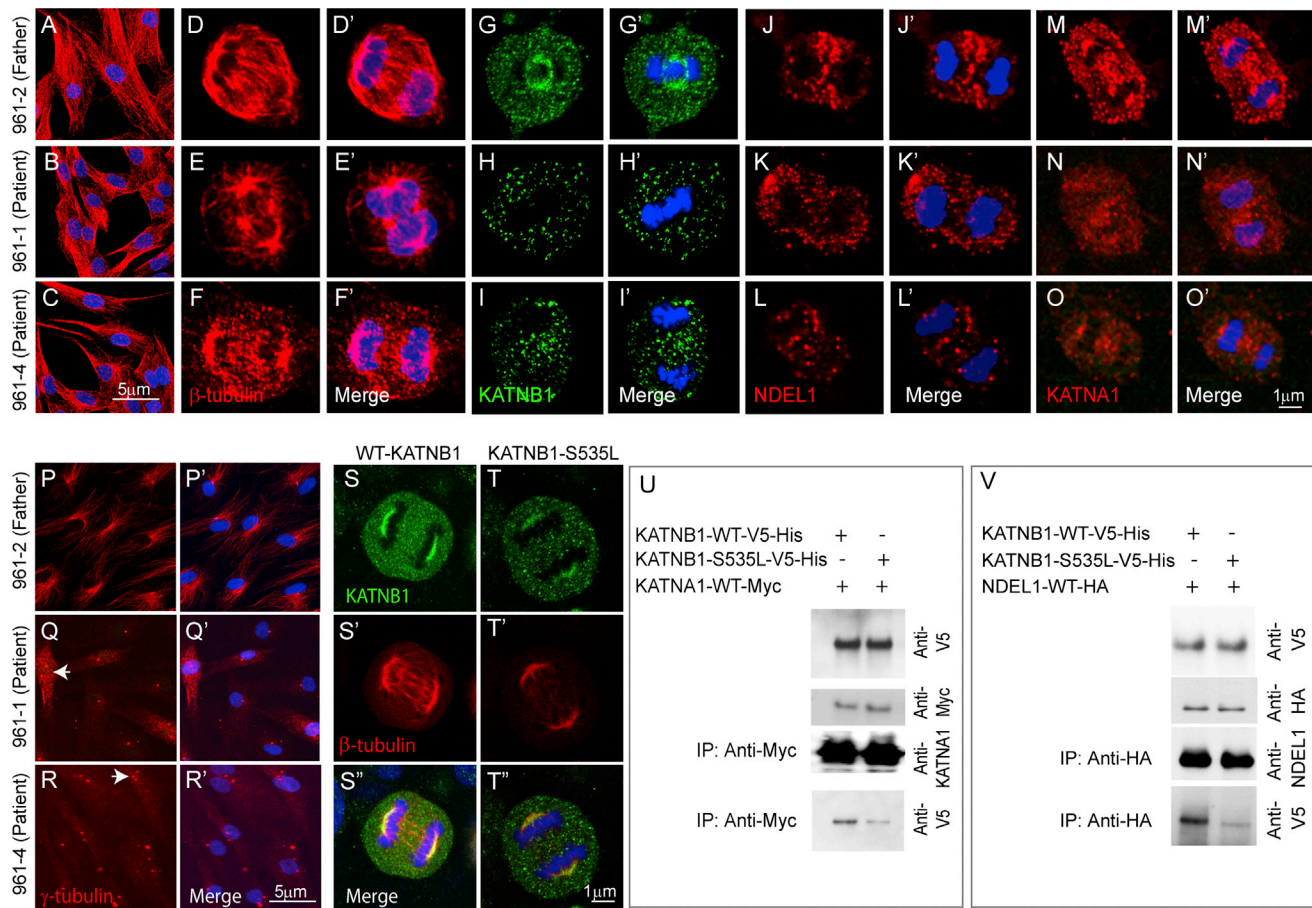


Figure 2. C-Terminal Mutant Forms of KATNB1 Disrupt the Mitotic Spindle and Display Reduced Interaction with NDEL1 and KATNA1

(A–C) As evidenced by β -tubulin staining, microtubule architecture of the interphase dermal fibroblasts, derived from patients and their parents, is intact. However, the mitotic spindle is significantly disrupted and malformed in patient-derived cells in anaphase (D–F). Patient fibroblasts also show reduced localization of KATNB1 (G–I), NDEL1 (J–L), and KATNA1 (M–O) to the mitotic spindle and increased number of centrosomes (arrow) as seen by staining for γ -tubulin (P–R). Panels marked with a prime (') show merged images of primary antigen and DAPI (blue) staining (D'–R'). Consistent with the observations in patient fibroblasts, transfection of HeLa cells with wild-type and mutant forms of KATNB1 results in reduced localization of mutant form of KATNB1 (green) to centrosomes and abnormal spindle formation (tubulin staining; red) in anaphase cells (S–T''). The specific KATNB1 mutation assayed/investigated is indicated at the top of the panel. Coimmunoprecipitation of wild-type and mutant forms of KATNB1 with KATNA1 (U) and NDEL1 (V) shows reduced interaction of mutant KATNB1 with both proteins. Scale bars, 5 μ m (A–C and P–R), 1 μ m (D–O, S, and T). All confocal images were captured using identical settings (see also Figure S2).

classic pachygyria (lissencephaly) and polymicrogyria, but resembles the cortical malformation seen in other severe congenital microcephaly syndromes, especially NDE1 (Alkuraya et al., 2011; Bakircioglu et al., 2011). At the genetic level, exome sequencing of these patients revealed all to harbor rare homozygous or compound heterozygous LOF, splice site, or predicted deleterious missense *KATNB1* mutations, including p.Val45Ileu, p.Val150Cysfs*22, p.Ser535Leu, p.Leu540Arg, and IVS9-1G > A;p.Gly578Asp (Figure 1; Table S1). All mutations were confirmed by Sanger sequencing and segregated as expected, with both parents of the affected children being heterozygous for the respective mutations. None of the mutations were observed in the public databases or among the 3,000 exomes sequenced at Yale including 1,460 ethnically matched control chromosomes. These findings provide conclusive evidence that mutations in *KATNB1* are the underlying genetic cause of the observed MCD phenotypes.

Mutations in *KATNB1* Disrupt Mitotic Spindle Architecture

To study the functional consequences of the *KATNB1* mutations at the cellular level, we used dermal fibroblast cultures established from skin biopsies of two patients (siblings NG-961-1 and NG-961-4, carrying the p.Ser535Leu mutation) and an unaffected heterozygous parent (NG-961-2). Western analysis revealed reduced KATNB1 (but not of its interactors) in patient-derived cells (Figure S2A) without an obvious impact on the microtubule network, as there were no apparent differences in either the intensity of KATNB1 immunostaining or the microtubule cytoskeleton in interphase cells (Figures 2A–2C). However, in dividing cells, the mutations affected the mitotic spindle with patient-derived cells displaying disorganized microtubules (Figures 2D–2F') and reduced KATNB1 immunostaining (Figures 2G–2I'). Since KATNB1 facilitates the recruitment of KATNA1 and its interactors, such as NDEL1, to target locations, we next investigated

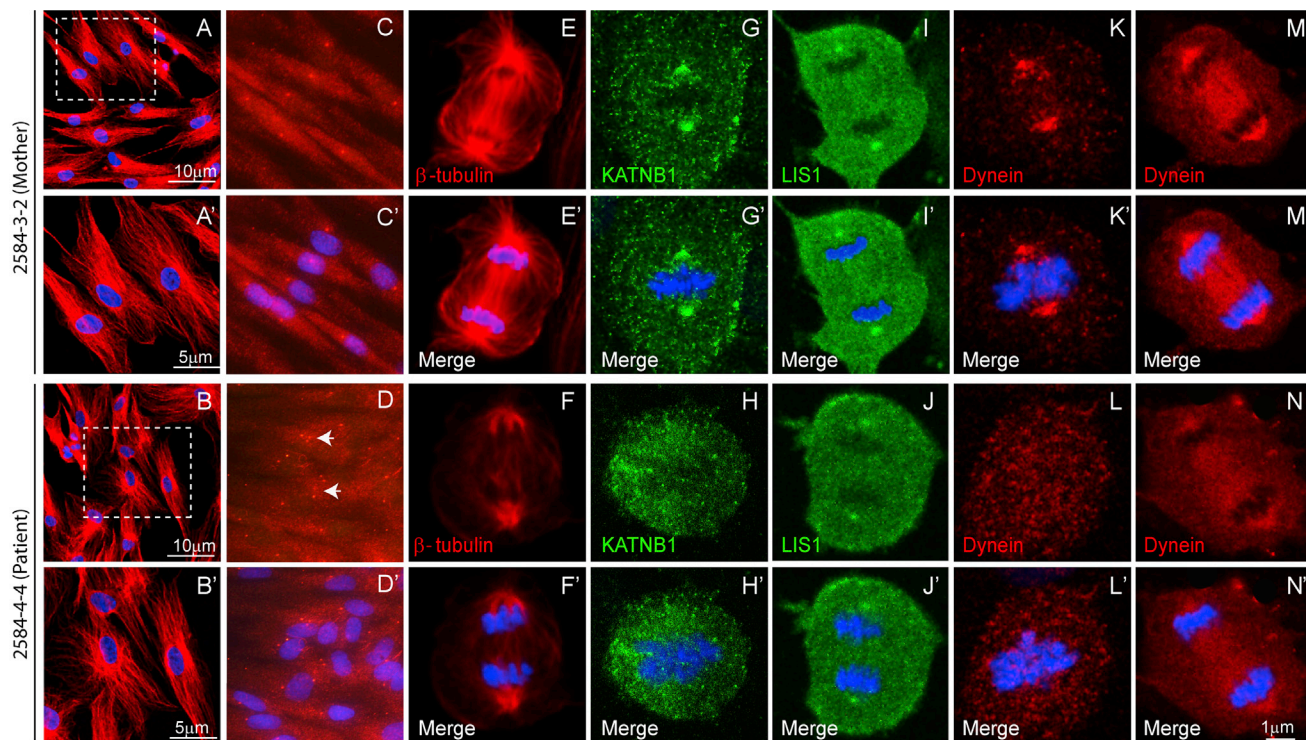


Figure 3. N-Terminal Mutant Forms of KATNB1 Display Reduced Interaction with Dynein and Disrupted Mitotic Spindle

β -tubulin staining shows microtubule architecture to be intact in interphase dermal fibroblasts derived from patients and their parents (A and B). However, patient-derived cells display increased number of centrosomes (arrow) as seen by staining for γ -tubulin (G and H) and significantly disrupted and malformed mitotic spindle in anaphase (E and F). Patient fibroblasts also show reduced localization of KATNB1 (G and H), LIS1 (I and J), and Dynein (K–N) to the mitotic spindle and spindle poles. Panels marked with a prime (') show merged images of primary antibody and DAPI (blue) staining (A'–N'). All confocal images were captured using identical settings.

NDEL1 and KATNA1 localization in mitotic cells and found both to be reduced in the mitotic spindle (Figures 2J–2L' and 2M–2O', respectively). Also, patient-derived fibroblasts displayed aberrant number of centrosomes (Figures 2P–2R'). Next, we expressed wild-type (WT) or mutant KATNB1 (p.Ser535Leu) in HeLa cells and found that tubulin staining of the mitotic spindle and localization of the mutant forms to the centrosomes were reduced, suggesting that the defect in KATNB1 is sufficient to cause mitotic spindle perturbation (Figures 2S–2T' and S2). Moreover, immunoprecipitation of HeLa cell lysates transfected with WT or mutant forms of KATNB1 along with KATNA1 or NDEL1 showed reduced interaction of the mutant forms of KATNB1 with both KATNA1 and NDEL1 (Figures 2U and 2V). This supports an essential role for the interaction of these proteins for their targeting to the mitotic spindle.

We also assessed the effect of N-terminal domain mutation in dermal fibroblast cultures from the index case of family NG-2584 (carrying the p.Val150Cysfs*22 mutation) and an unaffected parent. As with the p.Ser535Leu mutant fibroblasts, we failed to detect an impact of the mutation on microtubule architecture in interphase cells, but mitotic cells displayed spindle morphology defects (Figures 3A–3D') and supernumerary centrosomes (Figures 3C–3D'). In mitotic cells, spindle pole localization of KATNB1 was strikingly affected (Figures 3G–3H'), while that of LIS1 was slightly reduced (Figures 3I–3J'). Similarly, Dynein

levels at the spindle poles and the spindle proper were dramatically reduced (Figures 3K–3N').

KATNB1 Expression in the Developing Brain

The above findings demonstrate that KATNB1 mutations impact the overall spindle dynamics and integrity by affecting the assembly of the NDEL1/KATNA1/Dynein/LIS1 complex at the spindle poles and microtubules. To understand how these mutations lead to severe cortical abnormalities in humans, we next investigated KATNB1 expression in the developing human brain by interrogating the Human Brain Transcriptome Database (Kang et al., 2011) and found it to be stably expressed throughout fetal development, starting shortly after conception (Figure 4A). Expression levels remained elevated into infancy particularly in neocortex, hippocampus, and striatum, with high levels still detected in the adult brain. The high levels of expression and localization in neural progenitor cells and postmitotic neurons during early development suggest a continuing role of KATNB1 in neuronal proliferation, migration, and laminar organization of the human cortex.

We then investigated KATNB1 expression in the developing mouse and zebrafish brains. In mouse, *Katnb1* was initially expressed in neural progenitors until midneurogenesis, and subsequently in postmitotic neurons in the cortical plate; in postnatal brain, *Katnb1* was expressed widely (Figures 4B–4F). Similarly,

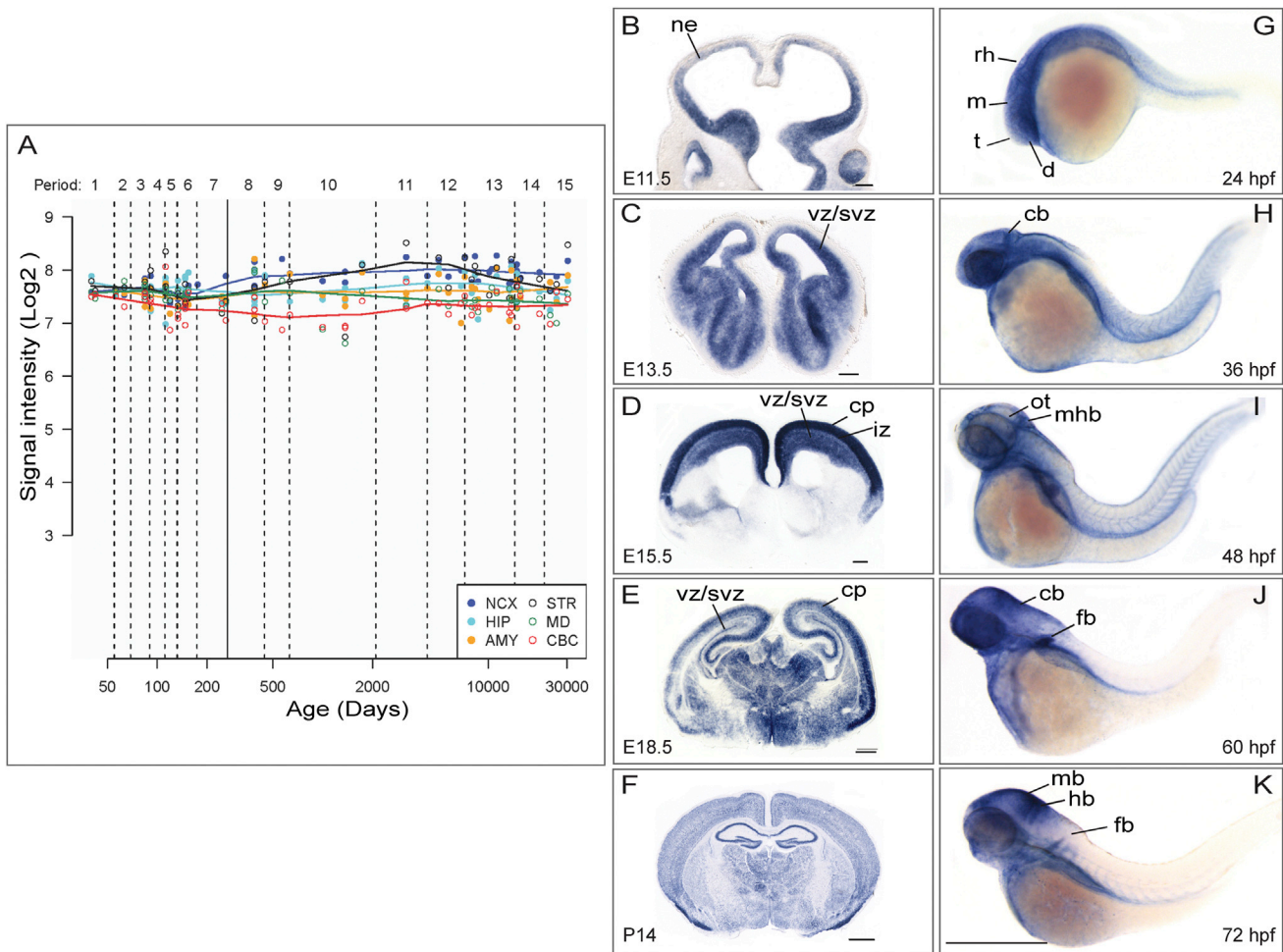


Figure 4. *KATNB1* Is Highly Expressed in the Developing Brain

(A) *KATNB1* is expressed across all regions and developmental periods in the human brain. *KATNB1* exon array signal intensity. NCX, neocortex; STR, striatum; HIP, hippocampus; MD, mediodorsal nucleus of the thalamus; AMY, amygdala; CBC, cerebellar cortex. In developing mouse brain, *Katnb1* is expressed in neural progenitors until midneurogenesis (E11.5, E13.5) (B and C), and then is also expressed in postmitotic neurons in the cortical plate (E15.5, E18.5) (D and E), and widespread expression was observed in postnatal brain (P14) (F). vz, ventricular zone; svz, subventricular zone; iz, intermediate zone; cp, cortical plate. Scale bars (G–I), 200 μ m, (J and K), 500 μ m. Similarly, *katnb1* is expressed in the brain in the developing zebrafish embryo (G–K). Lateral views of whole-mount in situ hybridization of the brain and torso of zebrafish embryos reveal the expression pattern of *katnb1* at 24 hr postfertilization (hpf) (G), 36 hpf (H), 48 hpf (I), 60 hpf (J), and 72 hpf (K). During early developmental stages (G and H), *katnb1* mRNA expression is ubiquitous throughout the embryo, including the cephalic region. As the embryos develop further (I–K), *katnb1* mRNA expression becomes restricted to neural tissue. Black lines point to various anatomical structures. d, diencephalon; t, telencephalon; m, mesencephalon; rh, rhombomeres; cb, cerebellum; ot, optic tectum; mhb, midbrain hindbrain boundary; mb, midbrain; hb, hindbrain; fb, fin bud. Scale bar, 500 μ m.

katnb1 was also highly expressed in the developing zebrafish brain. During early developmental stages, *katnb1* mRNA expression was ubiquitous throughout the embryo, including the cephalic region. As the embryo develops further, *katnb1* mRNA expression profile became more restricted (Figures 4G–4K).

Loss of *KATNB1* Orthologs in Zebrafish and *Drosophila* Results in Microcephaly

Based on the finding of diffuse *katnb1* expression in the developing zebrafish brain, we initially used this model organism to study *KATNB1* function. Knocking down *katnb1*, the single ortholog, by morpholino injection resulted in a significant reduction

of the midbrain size ($p = 9.16 \times 10^{-7}$) (Figures 5A–5E), recapitulating the major phenotypic finding in humans.

Next, to gain a detailed mechanistic insight into the biology of *KATNB1*, we extended our studies to *Drosophila*, a model that has been successfully implemented to study human MCD-associated genes. *kat80* (the single fly ortholog of human *KATNB1*; Goldstein and Gunawardena, 2000) has been shown to be ubiquitously expressed in both embryonic and larval stages (Chintapalli et al., 2007; Frise et al., 2010). To examine the potential role of *kat80* in regulating brain size, we employed the GAL4/UAS system (Xu and Rubin, 1993). We used Prospero-GAL4 to drive expression of *kat80* RNAi (*kat80-IR*) in neural progenitor cells

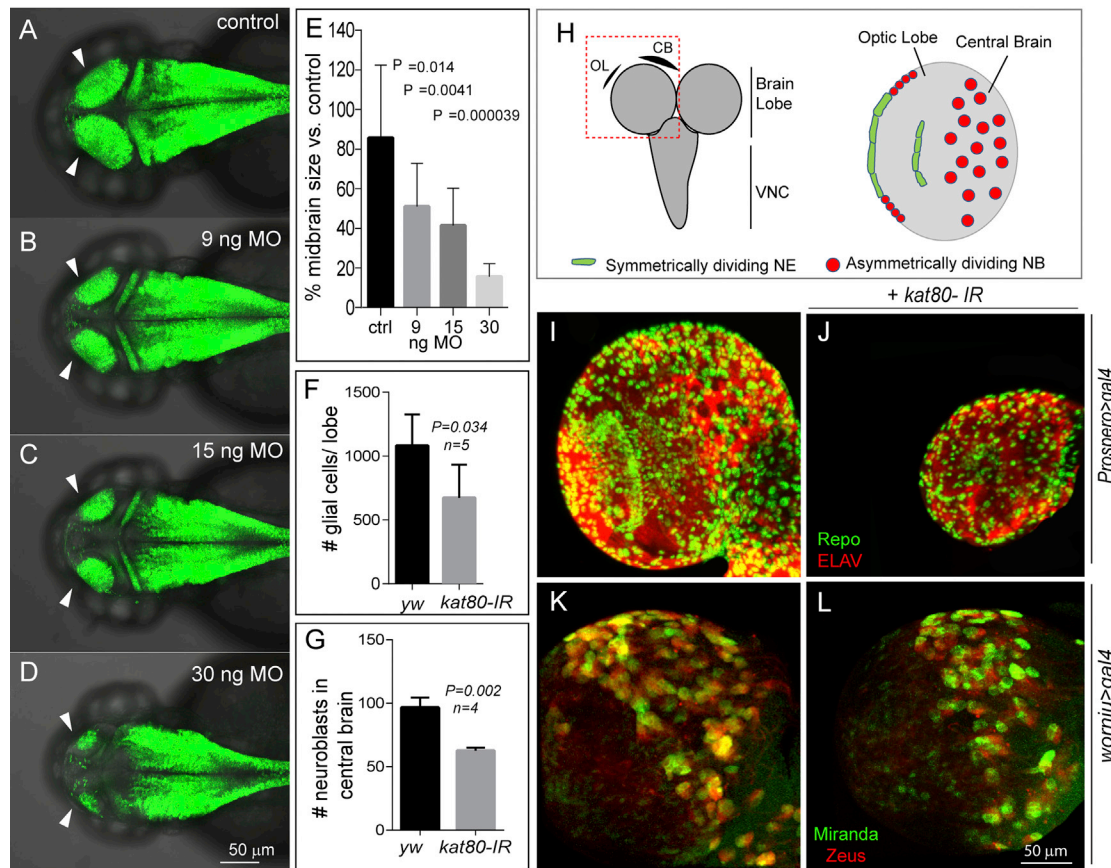


Figure 5. Knockdown of KATNB1 Orthologs in Zebrafish and Drosophila Results in Small Brain Phenotype

katnb1 morpholino reduces zebrafish midbrain size. Confocal microscopy shows that the *katnb1* morphants at (B) 9 nanograms (ng), (C) 15 ng, and (D) 30 ng have smaller midbrains (arrows) as compared with (A) control at 2 days postfertilization (dpf). The reduction in brain size is statistically significant (E). Zebrafish brain is labeled with green fluorescence by Tg (HuC:Kaede). (H) Left panel: schematic of the *Drosophila* brain; box indicates brain lobe imaged. Right panel: schematic of a single brain lobe marks the location of symmetrically dividing neuroepithelium (NE; green) and asymmetrically dividing neuroblasts (NBs; red). (I and J) Expression of *kat80-IR* with *prospero-Gal4* results in a dramatically reduced brain size in third instar larvae. There is an overall reduction in the number of neurons and glia generated as seen by ELAV (red) and Repo (green) staining, respectively. (K and L) *kat80-IR* expressed under *worniu-Gal4*, *UAS-mir::GFP*, *UAS-zeus::mCherry* results in a significant reduction in NB number in central brain. Images in (K) and (L) are 3D projections of identical Z-sections. (F) Quantification of glial cell counts seen in (I) and (J). There is significantly reduced number of glial cells in *kat80-IR* larvae (error bars indicate SD; *yw*, $1,080 \pm 110$; *kat80-IR*, 673 ± 116 ; two-tailed t test, $p = 0.034$). (G) GFP- and RFP-positive cells were quantified using 3D projections of identical Z-stacks from *worniu>gal4* and *worniu>kat80-IR* brains, which reveal a significant reduction in central brain NBs per brain lobe (*yw*, 96.5 ± 7.9 ; *kat80-IR*, 62.5 ± 2.3 ; $p = 0.002$) (see also Figure S3).

(NBs) and their newly born progeny (ganglion mother cells), which constitute the majority of cells in the developing larval brain (Figure 5H) (Isshiki et al., 2001). *kat80-IR* resulted in markedly reduced brain size (microcephaly) of third instar larvae as compared with controls (Figures 5I and 5J) with a concomitant reduction in the number of differentiated cells (Figure 5F) ($1,080 \pm 110$ versus 673 ± 116 in WT [*yw*] and *kat80-IR* flies, respectively; $p = 0.034$). Approximately 30% of the *kat80-IR* brains were reduced to one-tenth of normal size (Figure 5J).

***kat80* Loss in *Drosophila* Results in Mitotic Spindle Abnormalities, Delay in AO, and Mitotic Failure**

The above findings demonstrate that KATNB1 regulates neurogenesis in both vertebrates and invertebrates, but do not reveal the underlying molecular mechanism. As mutations affecting NB numbers are also known to impact brain size (Lee et al., 2006),

we next examined whether *kat80-IR*-expressing larval brains had fewer cells. Larval central brain NBs are specified during embryogenesis, then enter quiescence, progressively exiting during larval life to reach a total number of ~ 100 per brain lobe at third instar. NBs can be identified by their large size and expression of molecular markers, including the cell polarity protein Miranda (Mir) and transcription factor Worniu (Wor) (Ashraf et al., 2004; Lai et al., 2012). We used *Wor-GAL4* to express *kat80-IR* and GFP::Miranda to identify NBs and scored the number of Wor/Mir-positive cells. We found that third instar *kat80-IR* larval brains had on average ~ 70 NBs per lobe as compared to ~ 100 in WT brains (Figures 5G, 5K, and 5L; $p < 0.002$), indicating that *kat80* regulated brain size at least partly by controlling the NB number, which could be due to either excessive cell death or reduced cell proliferation. TUNEL staining showed no apparent ectopic cell death (Figures S3A–S3D'') in *kat80-IR*

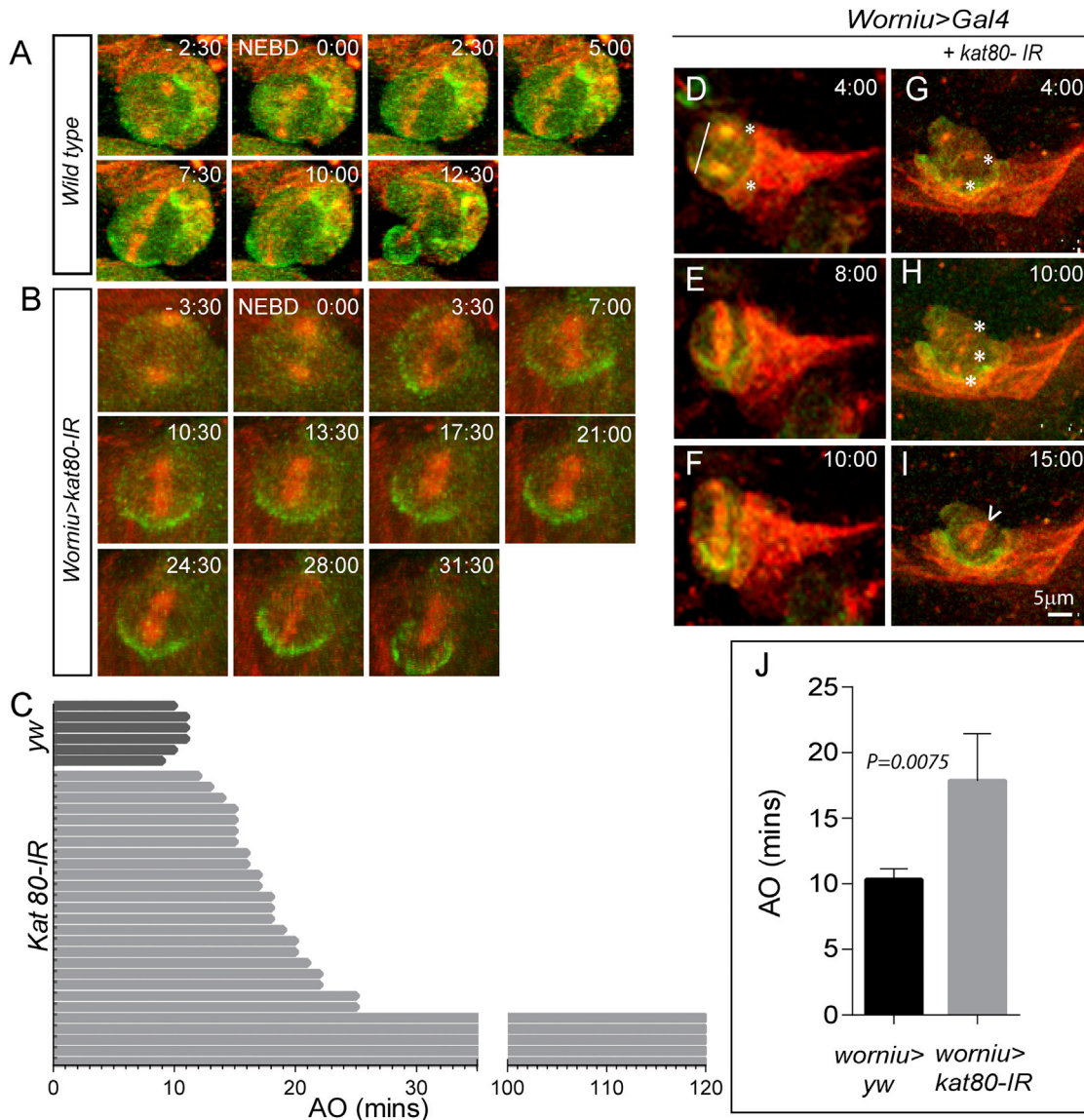


Figure 6. *kat80-IR* Delays Anaphase Onset in *Drosophila* Central Brain Neuroblasts, Causing a Reduction in Their Numbers

(A–C) *kat80-IR* was expressed under *worniu-Gal4*, *UAS-mir::GFP*, *UAS-zeus::mCherry*. Thirty NBs from *worniu>kat80-IR* and six NBs from *worniu>gal4* third instar larval brains were used for time-lapse imaging. Wild-type NBs exhibit anaphase onset at $\sim 10.33 \pm 0.82$ min after nuclear envelope breakdown. *kat80-IR* leads to increase in anaphase-onset time with an average of about 17.9 ± 3.59 min (error bars indicate SD; two-tailed t test, $p = 0.008$). In addition, four NBs failed to display anaphase onset even after 2 hr of imaging (C). Snapshots of live imaging of third instar larval brains expressing *kat80-IR* under *worniu > Gal4*, *mir-GFP*, *zeus-mcherry*. A wild-type (D–F) and a *kat80-IR* (G–I) NB undergoing division are shown. *kat80-IR* expression results in multiple centrosomes (asterisks in G and H) and multipolar and barrel-shaped spindles (arrowhead in I). (J) Quantification of time to anaphase onset of 30 *kat80-IR* NBs compared with wild-type (*yw*) cells reveals significant delay in mutant NBs.

clones, indicating that, at least in the third instar larvae, *kat80* knockdown affects brain size independently of cell death.

Given the impact of KATNB1 loss on mitotic spindle (Figures 2D–2F' and 3C–3D'), we postulated that in *kat80-IR* brains the remaining ~ 70 NBs could have cell cycle progression defects, further affecting the production of NB progeny and leading to microcephaly. Hence, we examined cell cycle progression in NBs using time-lapse imaging, and scored the time elapsed between nuclear envelope breakdown (NEBD; determined by the

initial detection of microtubules in the center of the cell) and AO (defined by the first sign of separation of sister chromatids), as previously described (Siller et al., 2005) (Figures 6A–6C and 6J). We made use of *Worniu-Gal4* to drive GFP::Miranda in order to mark the NBs and the microtubule-binding protein Zeus::mCherry to label the mitotic spindle. The NEBD-AO interval was significantly elongated in *kat80-IR* NBs as compared with controls (17.86 min \pm 3.59 min versus 10.33 min \pm 0.82 min, respectively; $p = 0.0075$), with AO extending over 2 hr in $\sim 13\%$

(n = 30) of *kat80-IR* NBs, indicating that *kat80* knockdown significantly delayed NB cell cycle progression.

Since patient-derived fibroblasts showed spindle and centrosome defects (Figures 2D–2F, 2P–2R, 3C, 3D, 3M, and 3N), we also examined *kat80-IR* NBs for similar abnormalities. We observed supernumerary centrosomes and multipolar and/or barrel-shaped spindles (Figures 6D–6I), suggesting that *kat80* regulates *Drosophila* brain size in vivo by controlling both number as well as cell cycle progression of NBs.

Differential Effects of *kat80* Loss in the Optic Lobe

Unlike the embryonically derived central brain NBs, those in the optic lobe are specified from neural epithelium (NE), which expands during larval life by undergoing symmetric divisions in the epithelial plane (Figure 5H). In contrast, optic lobe NB specification is accompanied by a coordinated switch from symmetric to asymmetric division (Figure 5E), a 90° rotation of the division axis, and expression of specific molecular markers (Egger et al., 2007, 2011; Homem and Knoblich, 2012). Thus, the optic lobe is ideal to study symmetrically versus asymmetrically dividing cells. We used *GH146-Gal4* to drive *kat80-IR* expression in the outer and inner proliferation centers of the optic lobe NE (Berdnik et al., 2008). Overall, no defects in NE morphology or spindle orientation were detected (Figures 7A–7E'), indicating that *kat80* does not regulate spindle integrity or cell cycle progression of symmetrically dividing NE cells. In sharp contrast, but similar to our observations in the central brain, the number of mitotic NBs (Mir-positive) was significantly reduced in the *kat80-IR*-expressing larval brains compared with controls (Figures 7F–7G' and 7J–7L). In addition, *kat80-IR* brains showed supernumerary centrosomes (average number/cell = 3) and twice as many cells in metaphase (57% ± 7% versus 26.9% ± 1.5% in *kat80-IR* versus WT [*yw*], respectively) (Figures 7H–7I' and 7M). These observations strongly suggested that *kat80* loss specifically affects asymmetrically dividing neural progenitor cells, at least in the *Drosophila* optic lobe.

Kat80 Loss Impacts on Dendritic Arborization

Finally, previous reports demonstrated changes in neuronal architecture and dendritic arborization not only in MCD patients (Barak et al., 2011; Kaindl et al., 2010), but also in other intellectual disability and related syndromes, including the Rett syndrome (Armstrong, 2005). Therefore, we studied potential neuronal structural abnormalities of the differentiated neurons in the *kat80-IR Drosophila* larvae. We examined the dendritic arborization (*da*) sensory neurons, which innervate the overlying larval epidermis and fall into four categories based on dendritic branching pattern and complexity (Grueber et al., 2007). Due to their accessibility and stereotyped morphology, *da* neurons serve as a model for dendritic growth, maintenance, and tiling (Jan and Jan, 2010). We used *pickpocket-Gal4* (*ppk-Gal4*) (Grueber et al., 2007) to drive *kat80-IR* expression in class IV *da* neurons, which are characterized by highly branched dendritic trees. In *kat80-IR Drosophila* larvae, dendritic arborization was dramatically reduced (Figures 8A and 8B), and the total number of dendritic termini was significantly diminished (Figure 8E; $p < 0.01$), suggesting that dendritic extension and number in peripheral neurons were compromised by *kat80* loss.

We next extended our observations to the *Drosophila* CNS by examining dendritic arborization of adult flight motoneurons (MN1–5) that innervate the dorsal longitudinal flight muscle (Consoulas et al., 2002; Ikeda and Koenig, 1988). Among all singly identifiable flight motoneurons, MN5 serves as a paradigm of dendritic architecture (Consoulas et al., 2002; Vonhoff and Duch, 2010). Using *D42-Gal4* to express *kat80-IR* primarily in adult flight motoneurons (Vonhoff and Duch, 2010) resulted in reduced dendritic arborization of MN5 (Figures 8C and 8D). Because dendritic defects in flight motoneurons alter flight performance (Vonhoff et al., 2012), we tested flight ability and found a significantly reduced flight response in adult *D42 > kat80-IR* versus WT flies (Figure 8F). Innervation of flight muscles was normal, as confirmed by imaging of MN axons and their targeting into the neuromuscular junction (NMJ) (Figures S5A and S5B). Further, although the number of boutons was not altered in the NMJ of *D42>kat80-IR* larvae, their diameter was significantly larger (Figures S5C–S5H), suggesting defective axonal transport. Finally, we did not detect any significant changes in axonal structure (data not shown). Taken together, these observations suggested that *kat80* regulates dendritic arborization of sensory and motor neurons in *Drosophila*.

DISCUSSION

Here, we report the identification of four homozygous deleterious mutations and one compound heterozygous deleterious mutation in *KATNB1* in multiple independent patients with pleomorphic cerebral cortical phenotypes of varying severity, consisting primarily of microlissencephalies, in which microcephaly co-occurred with neuronal migration abnormalities, ranging from white matter nodular heterotopia to lobar or global pachygyria, as well as cortical organization problems, including polymicrogyria.

KATNB1 encodes the p80 regulatory subunit of the microtubule-severing enzyme Katanin. A subset of the identified mutations (p.Leu540Arg, p.Ser535Leu, and p.Gly578Asp) localize to the C-terminal region of KATNB1, which is known to interact with the p60/KATNA1 catalytic subunit as well as NDEL1, while two mutations (p.Val45Ileu, p.Val150Cysfs*22) map to the N-terminal region, which interacts with the molecular motor protein Dynein and LIS1 (O'Donnell et al., 2012; Toyo-Oka et al., 2005). Patient-derived dermal fibroblasts displayed disorganized mitotic spindles and expressed lower amounts of KATNB1, similar to findings in the *Taily* mouse, which carries a hypomorphic allele of p80 (O'Donnell et al., 2012). The disease-causing mutations affect the interaction of KATNB1 with NDEL1 and KATNA1, disrupting their efficient localization to the centrosome and to the mitotic spindle during division. This is consistent with previous findings demonstrating that NDEL1 is required for Katanin localization to the centrosome during cell division (Toyo-Oka et al., 2005), suggesting that KATNB1, KATNA1, and NDEL1 are interdependent for their respective localization to the centrosomes. Similarly, fibroblasts harboring a N-terminal mutation in KATNB1 display spindle defects and a significant reduction in the amount of Dynein localizing to the spindle and centrosomes. Thus, *KATNB1* mutations result not only in decreased KATNB1 protein levels, but also

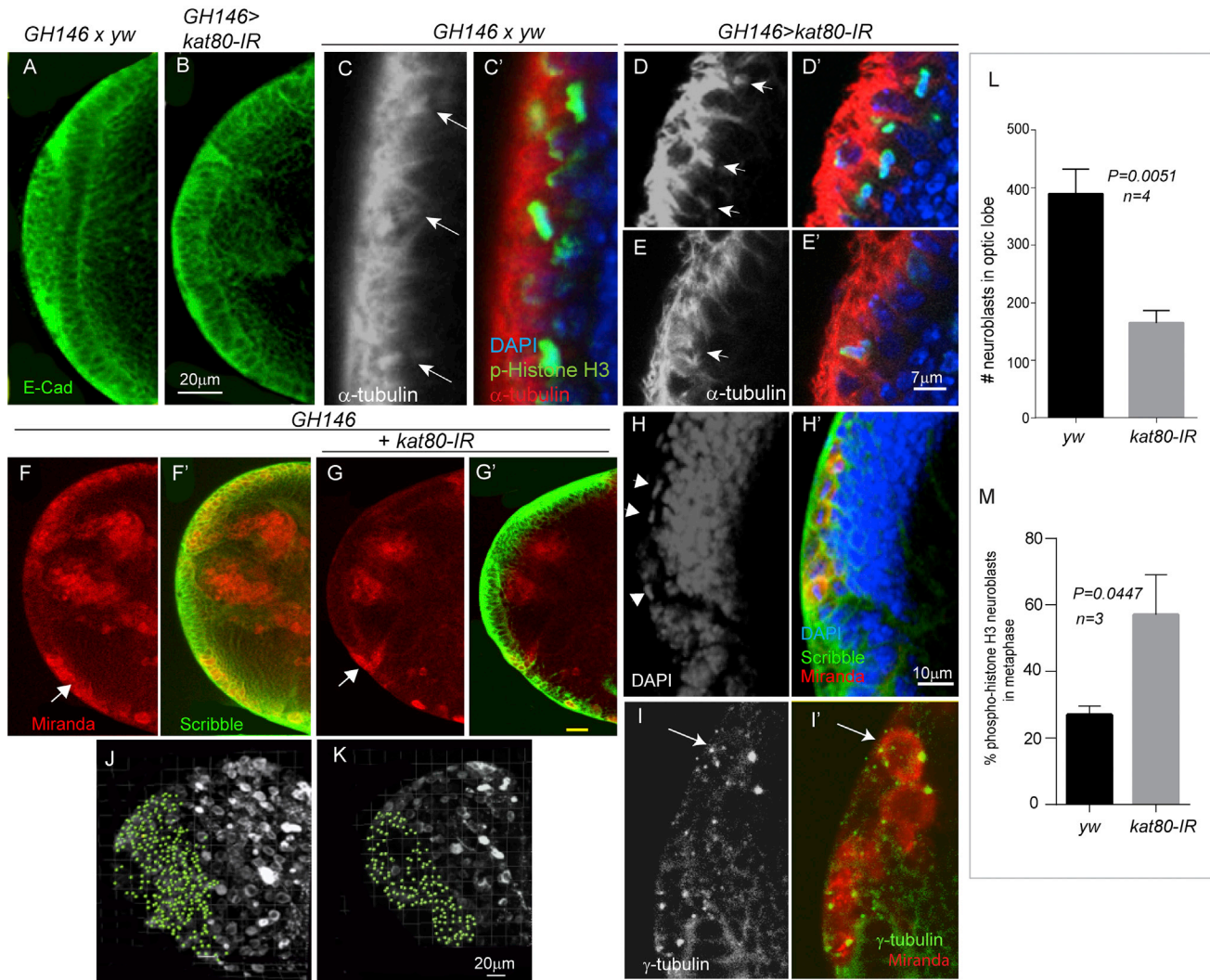


Figure 7. *kat80-IR* Results in Centrosomal Defects and Reduced Neuroblasts in *Drosophila* Optic Lobe

Expression of *kat80-IR* with *GH146-gal4* does not affect the morphology of the neuroepithelium (NE; marked by E-cadherin staining [green] in A and B) or spindle orientation (C–E). In (C)–(E), arrows marking the mitotic spindles and staining with alpha tubulin (red), phospho-histone H3 (pH3; marking the metaphase plate in the neuroepithelial cells; green), and DAPI (marking the nuclei; blue) are shown. (C)–(E) show α -tubulin staining only (gray scale) for easier visualization of the mitotic spindle. (F–G') Expression of *kat80-IR* in the optic lobe results in significantly reduced number of NBs (arrow). Miranda (marking NBs; red) and Scribble (marking NE cells) staining is shown in wild-type (*yw*; F and F') versus *kat80-IR* (G and G') larval brains. (H) and (H') are high-magnification images of the *kat80-IR* brain in (G), indicating that the NBs in *kat80-IR* brains are mainly in metaphase (arrowheads). (I and I') *GH146>kat80-IR* brains also show increased number of centrosomes in NBs as seen by gamma-tubulin staining (green) in miranda-positive NBs (red). (J and K) 3D projections of identical Z-sections of *GH146 > kat80-IR* and wild-type (*yw*) brains showing reduced number of Miranda-positive NBs in the optic lobe of third instar larval brains. (L) Quantification of the miranda-positive cells in the optic lobe shows significantly reduced NBs in the *kat80-IR* brains (mean \pm SEM; *yw*, 389 \pm 24.8; *kat80-IR*, 165 \pm 10.5; two-tailed t test, $p = 0.005$). (M) Quantification of phospho-histone H3 (pH3)-positive NBs in *kat80*-depleted brains shows an increase in the number of pH3-positive NBs in metaphase (also visible in H) (mean \pm SEM; *yw*, 26.9 \pm 1.5; *kat80-IR*, 57 \pm 7; two-tailed t test, $p = 0.04$) suggesting delayed anaphase onset (see also Figure S4).

reduced localization of the Katanin complex and other effector molecules to target areas, causing mitotic spindle defects.

To gain mechanistic understanding into KATNB1 function, we used *Drosophila*, a model system that has provided invaluable insight into the mechanism of action of genes involved in human MCD syndromes (Gonzalez et al., 1990; Liu et al., 2000; Rujano et al., 2013; Saunders et al., 1997; Siller and Doe, 2008; Yamamoto et al., 2014). Loss of the *KATNB1* ortholog results in microcephaly in both *Drosophila* and zebrafish, recapitulating the

human phenotype. In addition, in the accompanying paper by Hu et al., *Katnb1* knockout in mice leads to severe cortical abnormalities by affecting centriole and cilia biogenesis during development (Hu et al., 2014 [this issue of *Neuron*]).

In *Drosophila*, loss of *kat80* results in fewer NBs, which display cell cycle progression delay, ectopic supernumerary centrosomes, and aberrant mitotic spindles. The reduced NB numbers in central brain is most likely a result of their failing to exit quiescence. During mitosis, anaphase chromatid-to-pole motion is

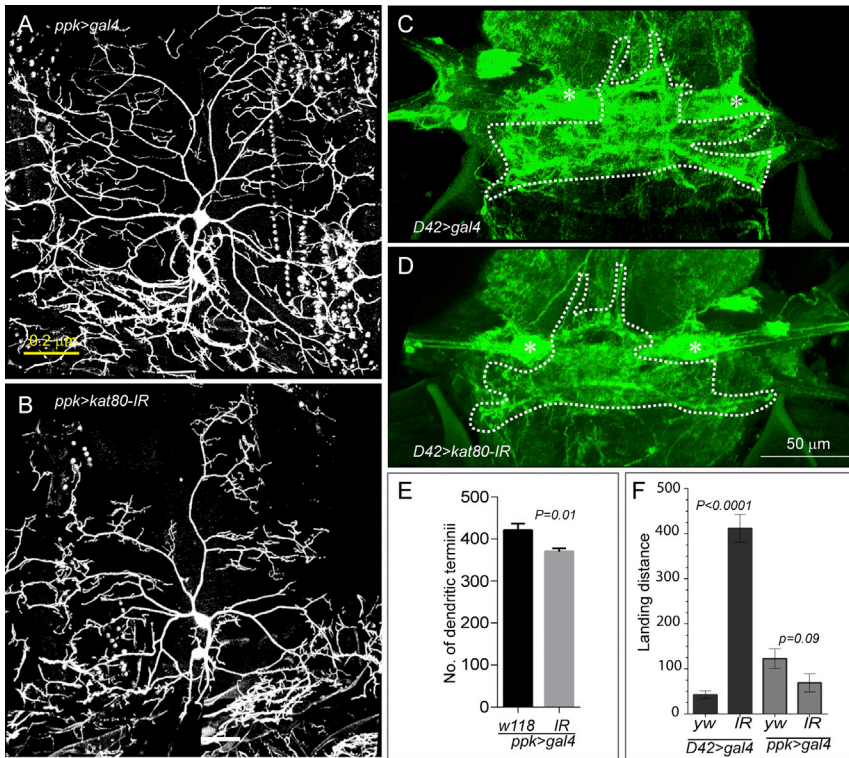


Figure 8. *kat80-IR* Results in Reduced Dendritic Arborization in Central and Peripheral Nervous System

(A and B) Larval class IV sensory neurons in the peripheral nervous system (PNS) were visualized using *UAS>CD8-GFP* expressed under the control of the *PPK-GAL4* driver. Morphological analysis of dendrites of class IV neurons, which display distinct morphology, was only performed in segments A3 and A4. We observed a significant reduction in dendrite extension in *kat80-IR* larvae (B) as compared to the wild-type, shown in (A). (C and D) *kat80-IR* reduced dendritic arbor of motoneuron 5 in the CNS (D) as compared to wild-type flies (C). Dendrites of adult flight motoneurons in the CNS were visualized by expressing *UAS>CD8-GFP* under the control of the *D42-GAL4* or *C380-GAL4* driver. Asterisk marks the motoneuron 5 cell body.

(E) The total number of terminal dendrites is statistically significantly reduced in *kat80-IR* versus wild-type larvae as counted manually on z-projections (mean \pm SEM; WT, 420 ± 15.67 ; *kat80-IR*, 369.6 ± 7.8 ; $p = 0.01$ [$n = 10$ cells, 7 larvae for WT, and $n = 10$ cells, 5 larvae for *kat80-IR* larvae]).

(F) The effect of reduced dendritic arborization of flight motoneurons was assessed in a flight assay. Expression of *kat80-IR* using the *D42* driver (expressed in adult motoneurons controlling wing muscles) resulted in severely impaired flight response, as assessed by the landing distance in the cylinder (left two columns in black, landing

distance in millimeters; mean \pm SEM; *D42* driver; WT [yw], 42.4 ± 8.7 ; *kat80-IR*, 411.7 ± 30.7 [$p = 0.0001$]). In contrast, *kat80-IR* expression in PNS sensory neurons under the *ppk* driver did not affect the flight response, as expected (right two columns in gray, landing distance in millimeters; *ppk* driver; mean \pm SEM; WT, 122.6 ± 21.8 ; *kat80-IR*, 69 ± 19.9). $n = 20$ adult males for each genotype (see also Figure S5).

tightly linked to depolymerization of the opposite ends of chromosome-associated microtubules. Synchronized microtubule dynamics result from the highly regulated, concerted action of several proteins, including *kat60* (Ghosh et al., 2012; Zhang et al., 2007). Since *kat80* is important for targeting the *kat60* catalytic subunit, our observation of delayed onset of anaphase in *kat80-IR* NBs further underscores the central role of Katanin in anaphase.

Unlike central brain NBs, which are derived from embryonic neural stem cells, the *Drosophila* optic lobe NBs originate from the neuroepithelium in a process that resembles the development of the vertebrate cerebral cortex, where progression from symmetric to asymmetric neurogenic divisions occur at early larval stages (Egger et al., 2007). Hence, *Drosophila* presents a unique system to dissect the molecular impact of any gene mutation on asymmetric versus symmetric cell division. For example, while *asp* loss leads to spindle defects and prometaphase arrest in central brain NBs, it causes chromosome segregation defects resulting in aneuploidy and apoptosis in optic lobe neuroepithelial cells (Gonzalez et al., 1990; Rujano et al., 2013; Saunders et al., 1997).

Surprisingly, *kat80* loss did not significantly impact symmetrically dividing progenitors in optic lobe NE, yet resulted in severe reduction of asymmetrically dividing NBs, clearly demonstrating the differential effects of *KATNB1* mutations on asymmetrically versus symmetrically dividing cells. The reduction in NB

numbers could be due to deregulation of signaling mechanisms that control NB specification, e.g., the Notch and JAK/STAT pathways. However, we found no effect of *kat80* loss on either pathway in the optic lobe (Figure S4), suggesting that *kat80* regulates NB numbers independent of these cues. Indeed, it is known that in the optic lobe, intracellular signaling events, and not spindle orientation, regulate NB specification and hence cell fate (Egger et al., 2007). Thus, in *kat80-IR* larvae, the deficit in optic lobe NBs is also likely due to a cell fate specification defect, a notion also supported by our observation that, at some frequency, we did indeed observe *kat80-IR* larvae with normal-size brains containing supernumerary NBs (K.M.-G., unpublished observations). This would suggest a role for Katanin in cell fate specification, which was previously shown to be independent of spindle orientation. Therefore, in the *Drosophila* larval brain, *kat80* plays a dual role such that its loss not only compromises the initial pool of cells per se (exit from quiescence or cell fate specification), but also their proliferative capability (delayed AO, spindle, and centrosomal defects), resulting in severe microcephaly.

Finally, microtubule severing and transport are known to play a central role in neuritogenesis (Franker and Hoogenraad, 2013). We observed a striking reduction of dendritic arborization of both central and peripheral neurons in *kat80-IR* flies, a finding that is consistent with the reported significant reduction of the dendritic field area and the number of the dendritic

termini in *kat-60L1* mutants (Stewart et al., 2012) and the role of Kat60 in dendritic elaboration (Mao et al., 2014). Dendrite pruning involves a noticeable degree of microtubule severing, especially in sensory neurons, and indeed MCDs have been associated previously with defective neuritogenesis (Gleeson et al., 1998; Shu et al., 2004). Furthermore, dendritic anomalies have been shown to be associated with intellectual disability (also seen in the patients reported here) and related syndromes caused by chromosomal aberrations (e.g., Down and Williams syndromes) and single gene mutations (e.g., Rett, Fragile-X, and Rubinstein-Taybi disorders) (Armstrong, 2005; Kaufmann and Moser, 2000).

Our findings demonstrate the fundamental importance of microtubule dynamics in brain development across species. Perturbation of this evolutionarily conserved cellular process leads to complex cerebral cortical malformations caused by abnormalities in microtubule severing. The successful identification of new genes, such as *KATNB1*, implicated in cerebral cortical development provides unique insights into how the human brain develops normally and how this process may be derailed. This clearly has a significant impact not only in the area of basic neuroscience, as it promises to reveal key players in the fundamental mechanisms that govern the development of the human brain, but also has implications for understanding the pathophysiology of common neurodevelopmental disorders.

EXPERIMENTAL PROCEDURES

Human Subjects and Animal Studies

The study protocol was approved by the Yale Human Investigation Committee (HIC) (protocol number 0908005592). Institutional review board approvals for genetic and MRI studies, along with written consent from all study subjects, were obtained by the referring physicians at the participating institutions. Upon fully informed consent, genomic DNA was extracted from peripheral blood samples of patients, their parents, and unaffected siblings, when available. DNA samples from affected individuals were subjected to whole-exome capture and sequencing, and to genome-wide genotyping for selected individuals. Identified mutations were confirmed and tested for segregation in the respective pedigrees by Sanger sequencing. For mouse work, mice were maintained in compliance with NIH guidelines and approval of the Yale University Institutional Animal Care and Use Committee. Embryos and adult fish were maintained under standard laboratory conditions, as approved by the University of California, San Diego Institutional Animal Care and Use Committee.

Fly Genetics

Oregon R or *yw* flies were used as WT controls. Other fly strains used include the following: *w;worniu-GAL4, UAS-Miranda::GFP, UAS-Zeus::mCHERRY/Cyo;Dr/TM6b* (Chris Doe); *w;UAS-CD8-GFP;D42-gal4,chagal80; c380-Gal4, UAS-CD8-GFP;;cha-gal80; hsFLP;Act-FRT-CD2-FRTgal4,UAS-CD8(n); y[1]w[1118]; P[w[+m]] = GawB}GH146* (Bloomington Stock Center); *kat80* RNAi lines were obtained from VDRC. Three independent *kat80* RNAi lines showed similar results.

Zebrafish Experiments

katnb1 morpholino was injected into one-cell-stage WT, and dorsal view images of 72 hpf control and morphant embryos were taken by a Leica M205 FA dissecting microscope with LAS AF software. Statistical analysis was carried out in Microsoft Excel.

All other experimental procedures are described in [Supplemental Experimental Procedures](#).

SUPPLEMENTAL INFORMATION

Supplemental Information includes five figures, one table, and Supplemental Experimental Procedures and can be found with this article online at <http://dx.doi.org/10.1016/j.neuron.2014.12.014>.

AUTHOR CONTRIBUTIONS

K.M.-G. designed, performed, and analyzed in vitro and in vivo (*Drosophila*) experiments to characterize the *KATNB1* mutations and wrote the manuscript. A.O.Ç. and A.E.S. performed genetic analysis, identified *KATNB1* mutations, and summarized the genetic, clinical, and radiological findings. C. Chabu helped design *Drosophila* experiments and write the manuscript and C. Chabu and T.X. helped analyze the data. O.H. generated and validated all constructs used in the study. F.V. worked on the dendritic arborization and bouton analysis studies and F.V. and H. Keshishian analyzed the data. G.T.A. experimentally verified human mutations. S.N. and W.H. performed expression analyses in mouse and human tissue and S.N., W.H., A.L., and N.S. analyzed the data. S.T. performed the zebrafish experiments and S.T. and N.C.C. analyzed the data. A.O.Ç., C.D., M.S.Z., H.A.A.H., J.-B.R., H.G., H. Kayserili, E.G.S., R.O.R., H.P., S.K., and W.B.D. ascertained and recruited patients, diagnosed and clinically evaluated patients, and collected samples. J.S. performed genetic investigation in patients. B.B., Caner Çağlar, Cagri Çağlar, D.D., and J.F.B. assisted in experimental work. F.J.M. performed radiological analysis. E.Z.E.-O. and K.Y. performed bioinformatic analysis. S.M.M. and R.P.L. oversaw exome sequencing of the patient samples. A.L. wrote the manuscript. K.B. analyzed the genetic data. J.G.G. analyzed the genetic data and led the research. M.G. analyzed the genetic data, wrote the manuscript, and led the research.

ACKNOWLEDGMENTS

We thank the patients and families who contributed to this study. This work was supported by the Yale Program on Neurogenetics and National Institutes of Health (NIH) Grants U54HG006504 (Yale Center for Mendelian Disorders, to R.P.L., M.G., M. Gerstein, and S.M.M.), U01MH081896 (to N.S.), and R01MH103616 (to M.G. and K.B.). This work was also supported by R01NS041537 and P01HD070494 (to J.G.G. and N.C.C.). R.P.L. and J.G.G. are Investigators of the Howard Hughes Medical Institute. We are grateful to the Gregory M. Kiez and Mehmet Kutman Foundation for continuing support.

Accepted: December 3, 2014

Published: December 17, 2014

REFERENCES

- Abdollahi, M.R., Morrison, E., Sirey, T., Molnar, Z., Hayward, B.E., Carr, I.M., Springell, K., Woods, C.G., Ahmed, M., Hattingh, L., et al. (2009). Mutation of the variant alpha-tubulin TUBA8 results in polymicrogyria with optic nerve hypoplasia. *Am. J. Hum. Genet.* **85**, 737–744.
- Ahmad, F.J., Yu, W., McNally, F.J., and Baas, P.W. (1999). An essential role for katanin in severing microtubules in the neuron. *J. Cell Biol.* **145**, 305–315.
- Alkuray, F.S., Cai, X., Emery, C., Mochida, G.H., Al-Dosari, M.S., Felie, J.M., Hill, R.S., Barry, B.J., Partlow, J.N., Gascon, G.G., et al. (2011). Human mutations in NDE1 cause extreme microcephaly with lissencephaly [corrected]. *Am. J. Hum. Genet.* **88**, 536–547.
- Armstrong, D.D. (2005). Neuropathology of Rett syndrome. *J. Child Neurol.* **20**, 747–753.
- Ashraf, S.I., Ganguly, A., Roote, J., and Ip, Y.T. (2004). Worniu, a snail family zinc-finger protein, is required for brain development in *Drosophila*. *Dev. Dyn.* **231**, 379–386.
- Bakircioglu, M., Carvalho, O.P., Khurshid, M., Cox, J.J., Tuysuz, B., Barak, T., Yilmaz, S., Caglayan, O., Dincer, A., Nicholas, A.K., et al. (2011). The essential role of centrosomal NDE1 in human cerebral cortex neurogenesis. *Am. J. Hum. Genet.* **88**, 523–535.

- Barak, T., Kwan, K.Y., Louvi, A., Demirbilek, V., Saygi, S., Tüysüz, B., Choi, M., Boyacı, H., Doerschner, K., Zhu, Y., et al. (2011). Recessive LAMC3 mutations cause malformations of occipital cortical development. *Nat. Genet.* **43**, 590–594.
- Barkovich, A.J., Guerrini, R., Kuzniecky, R.I., Jackson, G.D., and Dobyns, W.B. (2012). A developmental and genetic classification for malformations of cortical development: update 2012. *Brain* **135**, 1348–1369.
- Berdnik, D., Fan, A.P., Potter, C.J., and Luo, L. (2008). MicroRNA processing pathway regulates olfactory neuron morphogenesis. *Curr. Biol.* **18**, 1754–1759.
- Bettencourt-Dias, M., Hildebrandt, F., Pellman, D., Woods, G., and Godinho, S.A. (2011). Centrosomes and cilia in human disease. *Trends Genet.* **27**, 307–315.
- Bilgüvar, K., Oztürk, A.K., Louvi, A., Kwan, K.Y., Choi, M., Tatli, B., Yalnizoğlu, D., Tüysüz, B., Cağlayan, A.O., Gökben, S., et al. (2010). Whole-exome sequencing identifies recessive WDR62 mutations in severe brain malformations. *Nature* **467**, 207–210.
- Bond, J., Roberts, E., Springell, K., Lizarraga, S.B., Scott, S., Higgins, J., Hampshire, D.J., Morrison, E.E., Leal, G.F., Silva, E.O., et al. (2005). A centrosomal mechanism involving CDK5RAP2 and CENPJ controls brain size. *Nat. Genet.* **37**, 353–355.
- Casanova, M., Croub, L., Blaineau, C., Bourgeois, N., Bastien, P., and Pagès, M. (2009). Microtubule-severing proteins are involved in flagellar length control and mitosis in trypanosomatids. *Mol. Microbiol.* **71**, 1353–1370.
- Chintapalli, V.R., Wang, J., and Dow, J.A. (2007). Using FlyAtlas to identify better *Drosophila melanogaster* models of human disease. *Nat. Genet.* **39**, 715–720.
- Consoulas, C., Restifo, L.L., and Levine, R.B. (2002). Dendritic remodeling and growth of motoneurons during metamorphosis of *Drosophila melanogaster*. *J. Neurosci.* **22**, 4906–4917.
- Egger, B., Boone, J.Q., Stevens, N.R., Brand, A.H., and Doe, C.Q. (2007). Regulation of spindle orientation and neural stem cell fate in the *Drosophila* optic lobe. *Neural Dev.* **2**, 1.
- Egger, B., Gold, K.S., and Brand, A.H. (2011). Regulating the balance between symmetric and asymmetric stem cell division in the developing brain. *Fly (Austin)* **5**, 237–241.
- Franker, M.A., and Hoogenraad, C.C. (2013). Microtubule-based transport—basic mechanisms, traffic rules and role in neurological pathogenesis. *J. Cell Sci.* **126**, 2319–2329.
- Frise, E., Hammonds, A.S., and Celniker, S.E. (2010). Systematic image-driven analysis of the spatial *Drosophila* embryonic expression landscape. *Mol. Syst. Biol.* **6**, 345.
- Ghosh, D.K., Dasgupta, D., and Guha, A. (2012). Models, regulations, and functions of microtubule severing by Katanin. *ISRN Mol. Biol.* **2012**, 14.
- Gleeson, J.G., Allen, K.M., Fox, J.W., Lamperti, E.D., Berkovic, S., Scheffer, I., Cooper, E.C., Dobyns, W.B., Minnerath, S.R., Ross, M.E., and Walsh, C.A. (1998). Doublecortin, a brain-specific gene mutated in human X-linked lissencephaly and double cortex syndrome, encodes a putative signaling protein. *Cell* **92**, 63–72.
- Goldstein, L.S., and Gunawardena, S. (2000). Flying through the *Drosophila* cytoskeletal genome. *J. Cell Biol.* **150**, F63–F68.
- Gonzalez, C., Saunders, R.D., Casal, J., Molina, I., Carmena, M., Ripoll, P., and Glover, D.M. (1990). Mutations at the asp locus of *Drosophila* lead to multiple free centrosomes in syncytial embryos, but restrict centrosome duplication in larval neuroblasts. *J. Cell Sci.* **96**, 605–616.
- Grueber, W.B., Ye, B., Yang, C.H., Younger, S., Borden, K., Jan, L.Y., and Jan, Y.N. (2007). Projections of *Drosophila* multidendritic neurons in the central nervous system: links with peripheral dendrite morphology. *Development* **134**, 55–64.
- Hartman, J.J., Mahr, J., McNally, K., Okawa, K., Iwamatsu, A., Thomas, S., Cheesman, S., Heuser, J., Vale, R.D., and McNally, F.J. (1998). Katanin, a microtubule-severing protein, is a novel AAA ATPase that targets to the centrosome using a WD40-containing subunit. *Cell* **93**, 277–287.
- Hazan, J., Fonknechten, N., Mavel, D., Paternotte, C., Samson, D., Artiguenave, F., Davoine, C.S., Cruaud, C., Dürr, A., Wincker, P., et al. (1999). Spastin, a new AAA protein, is altered in the most frequent form of autosomal dominant spastic paraplegia. *Nat. Genet.* **23**, 296–303.
- Homem, C.C., and Knoblich, J.A. (2012). *Drosophila* neuroblasts: a model for stem cell biology. *Development* **139**, 4297–4310.
- Hu, W.F., Pomp, O., Kodani, A., Henke, K., Ben-Omran, T., Mochida, G.H., Yu, T.W., Woodworth, M.B., Bonnard, C., Shboul, M., et al. (2014). Katanin p80 regulates human cortical development by limiting centriole and cilia number. *Neuron* **84**, this issue, 1240–1257.
- Ikeda, K., and Koenig, J.H. (1988). Morphological identification of the motor neurons innervating the dorsal longitudinal flight muscle of *Drosophila melanogaster*. *J. Comp. Neurol.* **273**, 436–444.
- Isshiki, T., Pearson, B., Holbrook, S., and Doe, C.Q. (2001). *Drosophila* neuroblasts sequentially express transcription factors which specify the temporal identity of their neuronal progeny. *Cell* **106**, 511–521.
- Izraeli, S., Lowe, L.A., Bertness, V.L., Good, D.J., Dorward, D.W., Kirsch, I.R., and Kuehn, M.R. (1999). The SIL gene is required for mouse embryonic axial development and left-right specification. *Nature* **399**, 691–694.
- Jaglin, X.H., Poirier, K., Saillour, Y., Buhler, E., Tian, G., Bahi-Buisson, N., Fallet-Bianco, C., Phan-Dinh-Tuy, F., Kong, X.P., Bomont, P., et al. (2009). Mutations in the beta-tubulin gene TUBB2B result in asymmetrical polymicrogyria. *Nat. Genet.* **41**, 746–752.
- Jan, Y.N., and Jan, L.Y. (2010). Branching out: mechanisms of dendritic arborization. *Nat. Rev. Neurosci.* **11**, 316–328.
- Kaindl, A.M., Passemard, S., Kumar, P., Kraemer, N., Issa, L., Zwirner, A., Gerard, B., Verloes, A., Mani, S., and Gressens, P. (2010). Many roads lead to primary autosomal recessive microcephaly. *Prog. Neurobiol.* **90**, 363–383.
- Kang, H.J., Kawasawa, Y.I., Cheng, F., Zhu, Y., Xu, X., Li, M., Sousa, A.M., Pletikos, M., Meyer, K.A., Sedmak, G., et al. (2011). Spatio-temporal transcriptome of the human brain. *Nature* **478**, 483–489.
- Karabay, A., Yu, W., Solowska, J.M., Baird, D.H., and Baas, P.W. (2004). Axonal growth is sensitive to the levels of katanin, a protein that severs microtubules. *J. Neurosci.* **24**, 5778–5788.
- Kaufmann, W.E., and Moser, H.W. (2000). Dendritic anomalies in disorders associated with mental retardation. *Cereb. Cortex* **10**, 981–991.
- Kumar, R.A., Pilz, D.T., Babatz, T.D., Cushion, T.D., Harvey, K., Topf, M., Yates, L., Robb, S., Uyanik, G., Mancini, G.M., et al. (2010). TUBA1A mutations cause wide spectrum lissencephaly (smooth brain) and suggest that multiple neuronal migration pathways converge on alpha tubulins. *Hum. Mol. Genet.* **19**, 2817–2827.
- Lai, S.L., Miller, M.R., Robinson, K.J., and Doe, C.Q. (2012). The Snail family member Worniu is continuously required in neuroblasts to prevent Eglav-induced premature differentiation. *Dev. Cell* **23**, 849–857.
- Lee, C.Y., Robinson, K.J., and Doe, C.Q. (2006). Lgl, Pins and aPKC regulate neuroblast self-renewal versus differentiation. *Nature* **439**, 594–598.
- Liu, Z., Steward, R., and Luo, L. (2000). *Drosophila* Lis1 is required for neuroblast proliferation, dendritic elaboration and axonal transport. *Nat. Cell Biol.* **2**, 776–783.
- Mao, C.X., Xiong, Y., Xiong, Z., Wang, Q., Zhang, Y.Q., and Jin, S. (2014). Microtubule-severing protein Katanin regulates neuromuscular junction development and dendritic elaboration in *Drosophila*. *Development* **141**, 1064–1074.
- McNally, F.J., and Vale, R.D. (1993). Identification of katanin, an ATPase that severs and disassembles stable microtubules. *Cell* **75**, 419–429.
- McNally, K.P., Bazirgan, O.A., and McNally, F.J. (2000). Two domains of p80 katanin regulate microtubule severing and spindle pole targeting by p60 katanin. *J. Cell Sci.* **113**, 1623–1633.
- McNally, K., Audhya, A., Oegema, K., and McNally, F.J. (2006). Katanin controls mitotic and meiotic spindle length. *J. Cell Biol.* **175**, 881–891.
- O'Donnell, L., Rhodes, D., Smith, S.J., Merriner, D.J., Clark, B.J., Borg, C., Whittle, B., O'Connor, A.E., Smith, L.B., McNally, F.J., et al. (2012). An

- essential role for katanin p80 and microtubule severing in male gamete production. *PLoS Genet.* 8, e1002698.
- Pfaff, K.L., Straub, C.T., Chiang, K., Bear, D.M., Zhou, Y., and Zon, L.I. (2007). The zebra fish *cassiopeia* mutant reveals that SIL is required for mitotic spindle organization. *Mol. Cell Biol.* 27, 5887–5897.
- Reiner, O., Carrozzo, R., Shen, Y., Wehnert, M., Faustinella, F., Dobyns, W.B., Caskey, C.T., and Ledbetter, D.H. (1993). Isolation of a Miller-Dieker lissencephaly gene containing G protein beta-subunit-like repeats. *Nature* 364, 717–721.
- Rujano, M.A., Sanchez-Pulido, L., Penetier, C., le Dez, G., and Basto, R. (2013). The microcephaly protein Asp regulates neuroepithelium morphogenesis by controlling the spatial distribution of myosin II. *Nat. Cell Biol.* 15, 1294–1306.
- Saunders, R.D., Avides, M.C., Howard, T., Gonzalez, C., and Glover, D.M. (1997). The *Drosophila* gene abnormal spindle encodes a novel microtubule-associated protein that associates with the polar regions of the mitotic spindle. *J. Cell Biol.* 137, 881–890.
- Sharma, N., Bryant, J., Wloga, D., Donaldson, R., Davis, R.C., Jerka-Dziadosz, M., and Gaertig, J. (2007). Katanin regulates dynamics of microtubules and biogenesis of motile cilia. *J. Cell Biol.* 178, 1065–1079.
- Shu, T., Ayala, R., Nguyen, M.D., Xie, Z., Gleeson, J.G., and Tsai, L.H. (2004). Ndel1 operates in a common pathway with LIS1 and cytoplasmic dynein to regulate cortical neuronal positioning. *Neuron* 44, 263–277.
- Siller, K.H., and Doe, C.Q. (2008). Lis1/dynactin regulates metaphase spindle orientation in *Drosophila* neuroblasts. *Dev. Biol.* 319, 1–9.
- Siller, K.H., Serr, M., Steward, R., Hays, T.S., and Doe, C.Q. (2005). Live imaging of *Drosophila* brain neuroblasts reveals a role for Lis1/dynactin in spindle assembly and mitotic checkpoint control. *Mol. Biol. Cell* 16, 5127–5140.
- Stewart, A., Tsubouchi, A., Rolls, M.M., Tracey, W.D., and Sherwood, N.T. (2012). Katanin p60-like1 promotes microtubule growth and terminal dendrite stability in the larval class IV sensory neurons of *Drosophila*. *J. Neurosci.* 32, 11631–11642.
- Tanaka, T., Serneo, F.F., Higgins, C., Gambello, M.J., Wynshaw-Boris, A., and Gleeson, J.G. (2004). Lis1 and doublecortin function with dynein to mediate coupling of the nucleus to the centrosome in neuronal migration. *J. Cell Biol.* 165, 709–721.
- Thornton, G.K., and Woods, C.G. (2009). Primary microcephaly: do all roads lead to Rome? *Trends Genet.* 25, 501–510.
- Tischfield, M.A., Baris, H.N., Wu, C., Rudolph, G., Van Maldergem, L., He, W., Chan, W.M., Andrews, C., Demer, J.L., Robertson, R.L., et al. (2010). Human TUBB3 mutations perturb microtubule dynamics, kinesin interactions, and axon guidance. *Cell* 140, 74–87.
- Toyo-Oka, K., Sasaki, S., Yano, Y., Mori, D., Kobayashi, T., Toyoshima, Y.Y., Tokuoka, S.M., Ishii, S., Shimizu, T., Muramatsu, M., et al. (2005). Recruitment of katanin p60 by phosphorylated NDEL1, an LIS1 interacting protein, is essential for mitotic cell division and neuronal migration. *Hum. Mol. Genet.* 14, 3113–3128.
- Vonhoff, F., and Duch, C. (2010). Tiling among stereotyped dendritic branches in an identified *Drosophila* motoneuron. *J. Comp. Neurol.* 518, 2169–2185.
- Vonhoff, F., Williams, A., Ryglewski, S., and Duch, C. (2012). *Drosophila* as a model for MECP2 gain of function in neurons. *PLoS ONE* 7, e31835.
- Wakefield, J.G., Bonaccorsi, S., and Gatti, M. (2001). The *Drosophila* protein asp is involved in microtubule organization during spindle formation and cytokinesis. *J. Cell Biol.* 153, 637–648.
- Wieck, G., Leventer, R.J., Squier, W.M., Jansen, A., Andermann, E., Dubeau, F., Ramazzotti, A., Guerrini, R., and Dobyns, W.B. (2005). Periventricular nodular heterotopia with overlying polymicrogyria. *Brain* 128, 2811–2821.
- Xu, T., and Rubin, G.M. (1993). Analysis of genetic mosaics in developing and adult *Drosophila* tissues. *Development* 117, 1223–1237.
- Yamamoto, S., Jaiswal, M., Charrng, W.L., Gambin, T., Karaca, E., Mirzaa, G., Wiszniewski, W., Sandoval, H., Haelterman, N.A., Xiong, B., et al. (2014). A *Drosophila* genetic resource of mutants to study mechanisms underlying human genetic diseases. *Cell* 159, 200–214.
- Yu, W., Qiang, L., Solowska, J.M., Karabay, A., Korulu, S., and Baas, P.W. (2008). The microtubule-severing proteins spastin and katanin participate differently in the formation of axonal branches. *Mol. Biol. Cell* 19, 1485–1498.
- Zhang, D., Rogers, G.C., Buster, D.W., and Sharp, D.J. (2007). Three microtubule severing enzymes contribute to the “Pacman-flux” machinery that moves chromosomes. *J. Cell Biol.* 177, 231–242.

Neuron, Volume 84

Supplemental Information

Mutations in *KATNB1* Cause Complex

Cerebral Malformations by Disrupting

Asymmetrically Dividing Neural Progenitors

Ketu Mishra-Gorur, Ahmet Okay Çağlayan, Ashleigh E. Schaffer, Chiswili Chabu, Octavian Henegariu, Fernando Vonhoff, Gözde Tuğce Akgümüş, Sayoko Nishimura, Wenqi Han, Shu Tu, Burcin Baran, Hakan Gumus, Cengiz Dilber, Maha S. Zaki, Heba A.A. Hossni, Jean-Baptiste Rivière, Hülya Kayserili, Emily G. Spencer, Rasim O. Rosti, Jana Schroth, Hüseyin Per, Caner Çağlar, Cagri Çağlar, Duygu Dölen, Jacob F. Baranoski, Sefer Kumandaş, Frank J. Minja, E. Zeynep Erson-Omay, Shrikant M. Mane, Richard P. Lifton, Tian Xu, Haig Keshishian, William B Dobyns, Neil C. Chi, Nenad Šestan, Angeliki Louvi, Kaya Bilgüvar, Katsuhito Yasuno, Joseph G. Gleeson, and Murat Günel

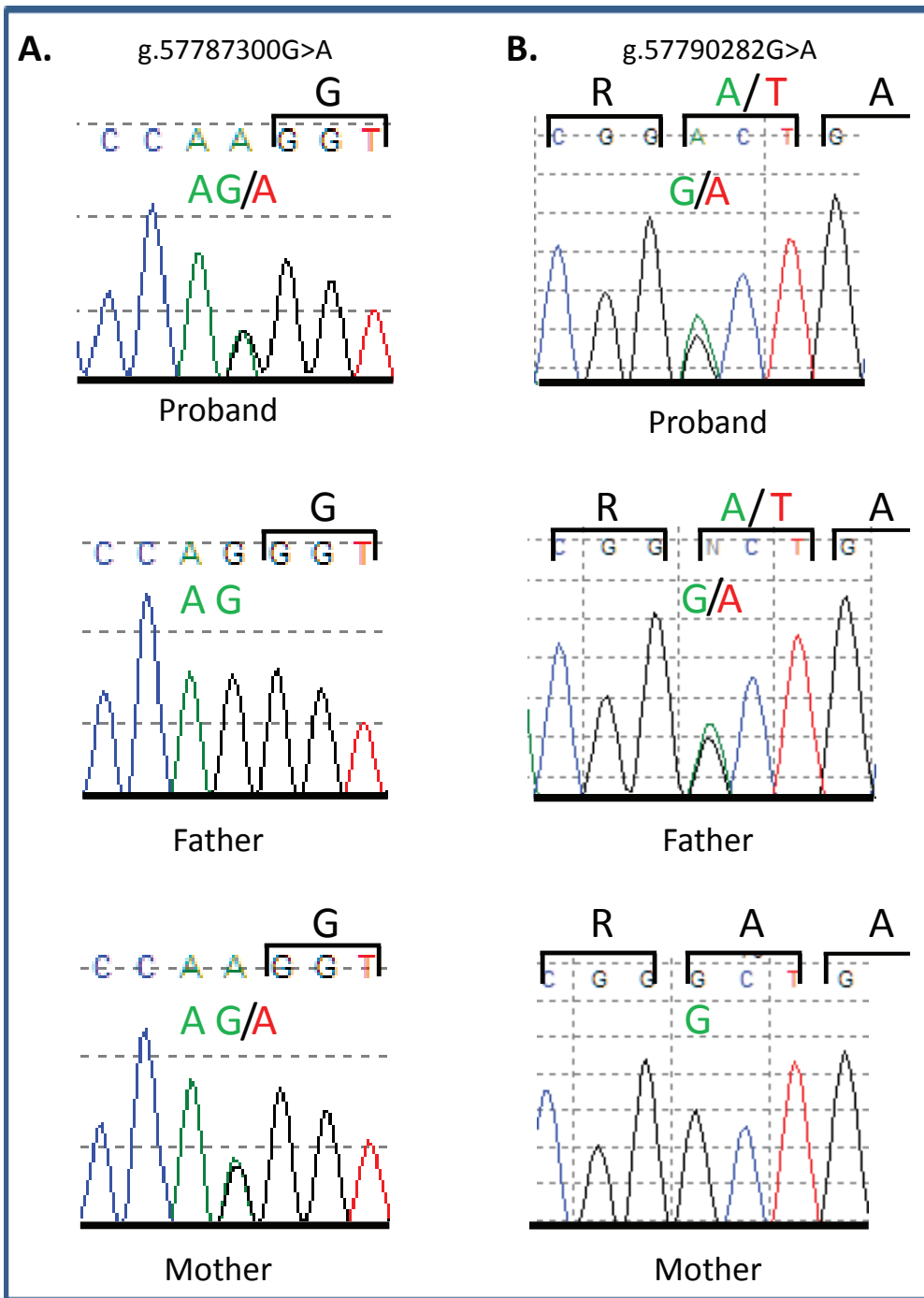


Figure S1
(Related to Figure 1)

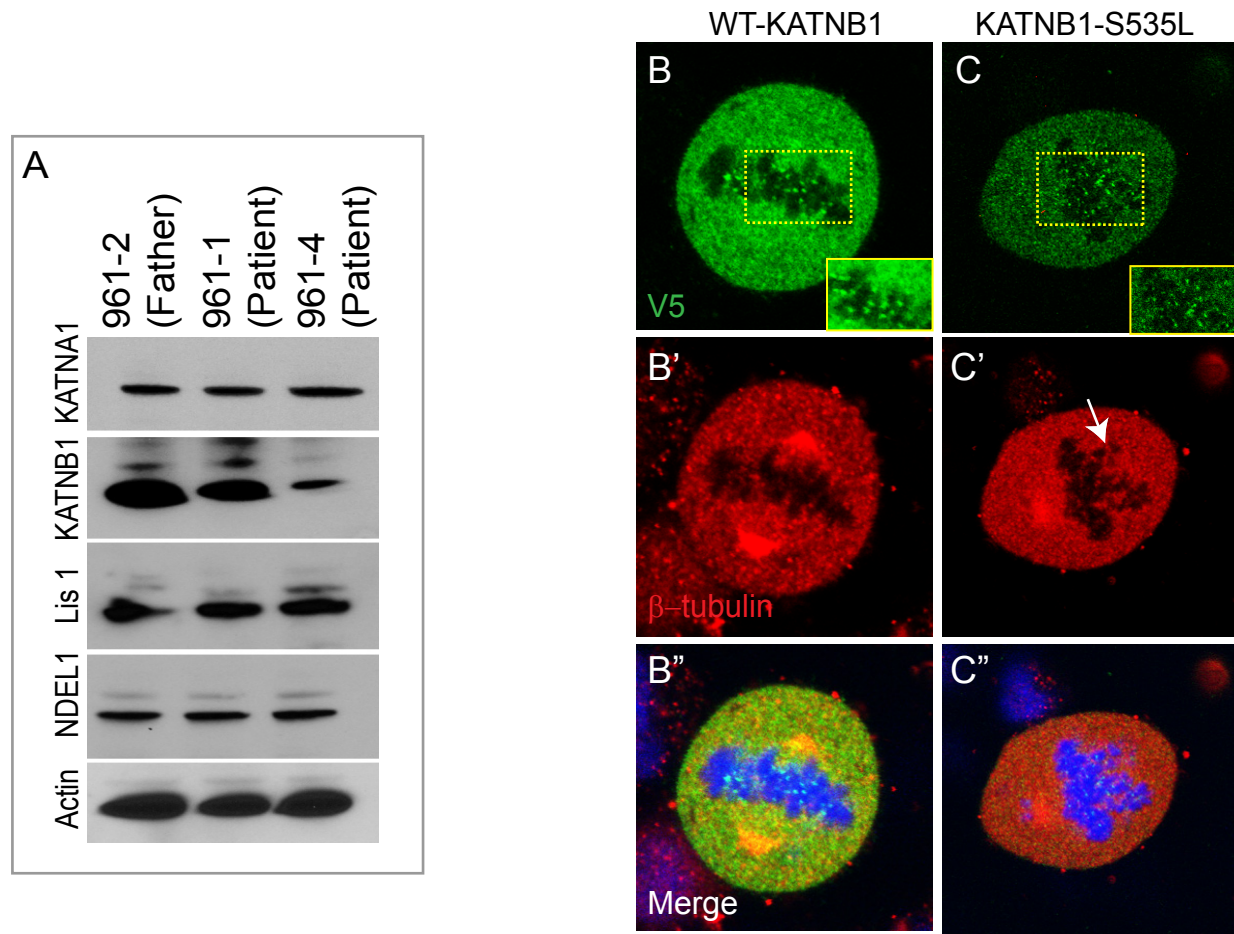


Figure S2
(Related to Figure 3)

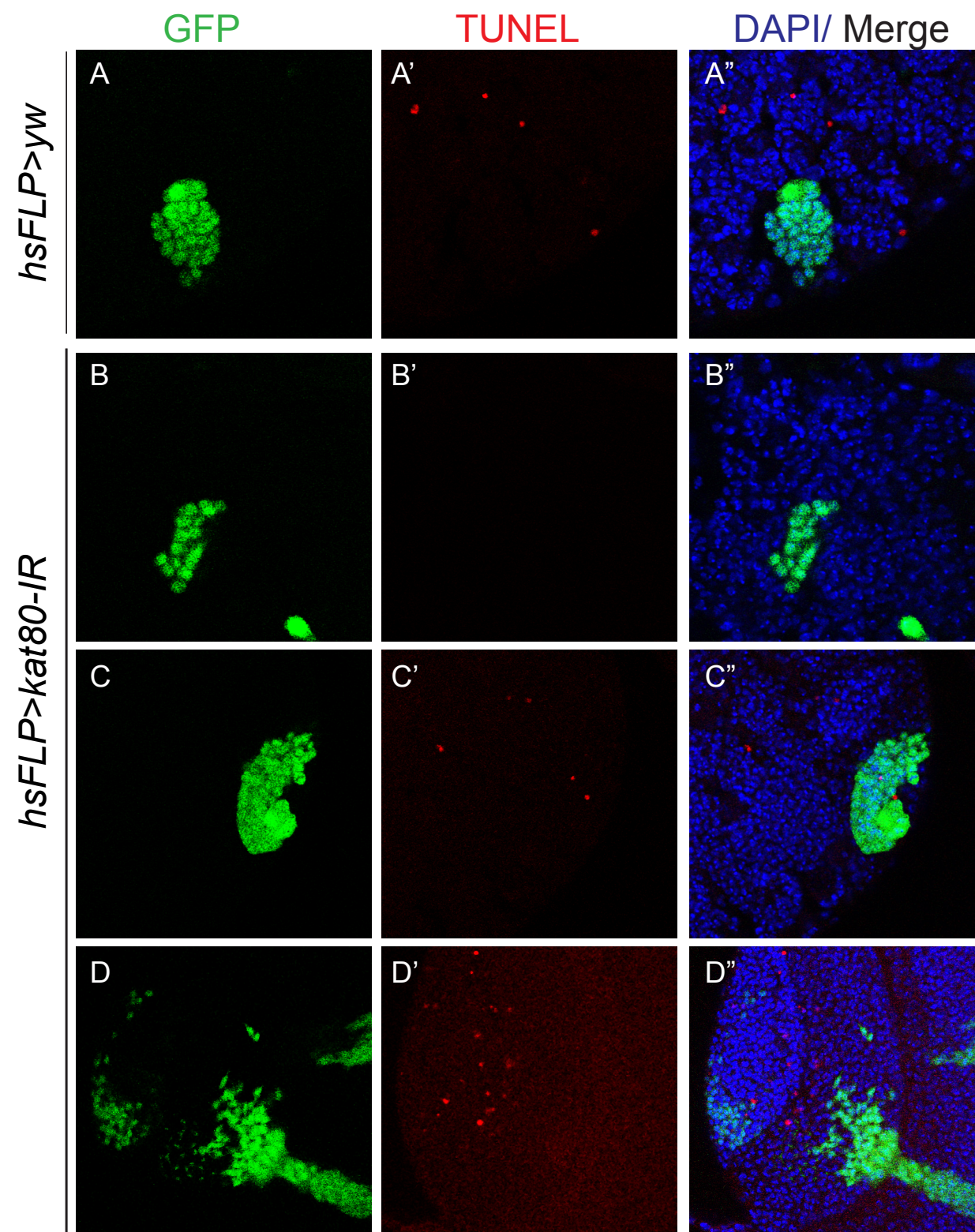


Figure S3
(Related to Figure 5)

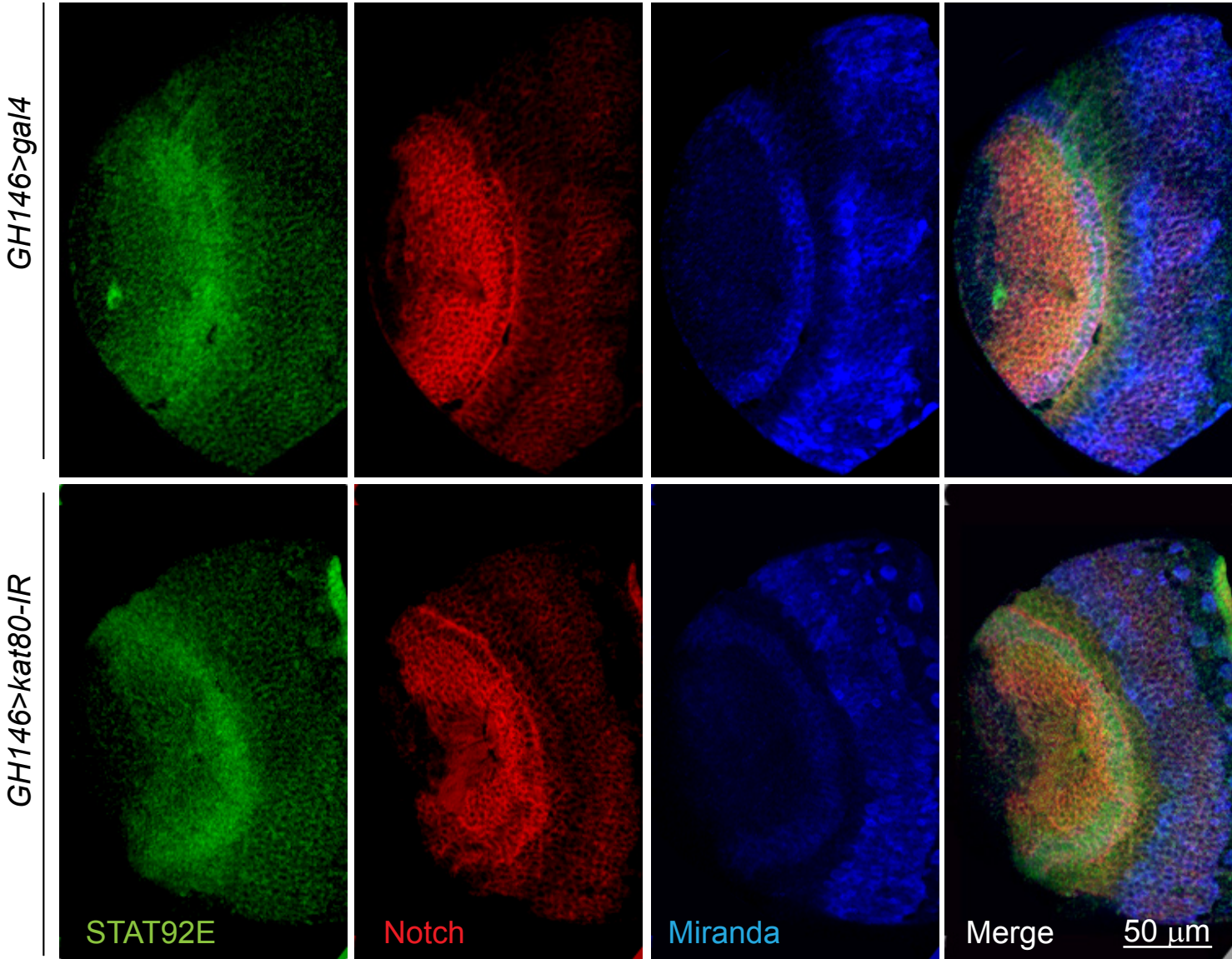
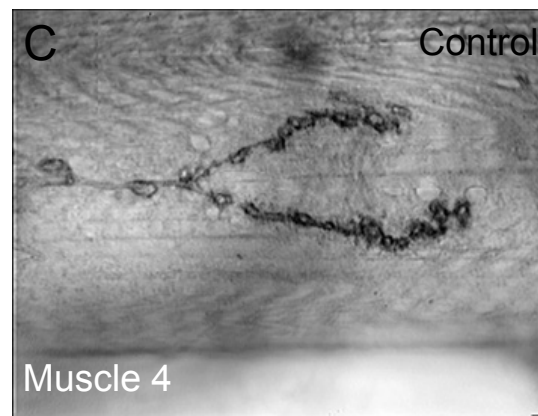
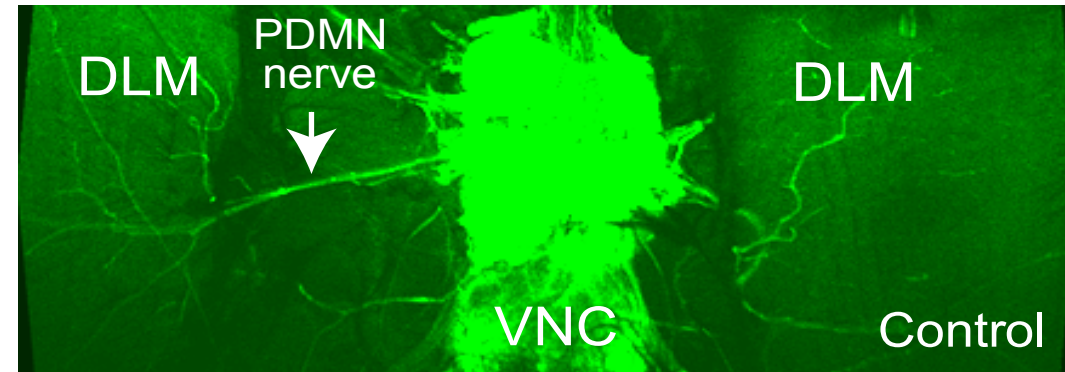
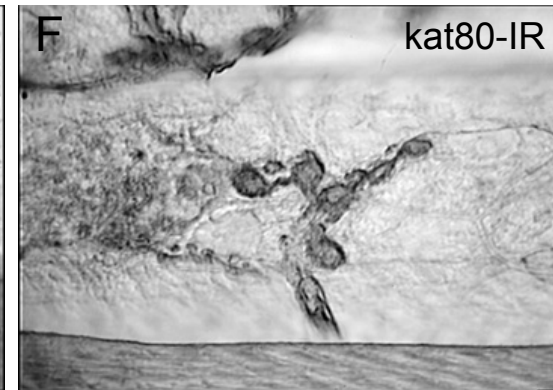
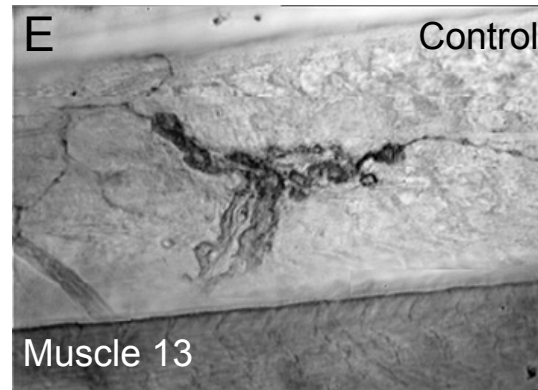
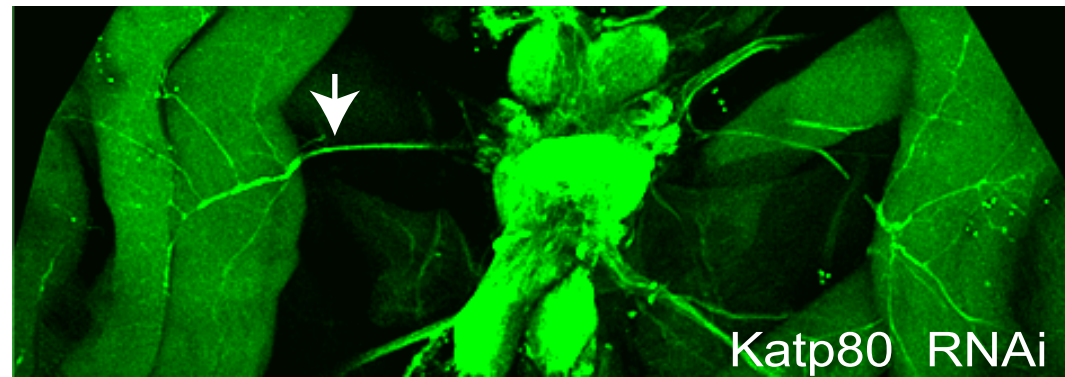


Figure S4
(Related to Figure 7)

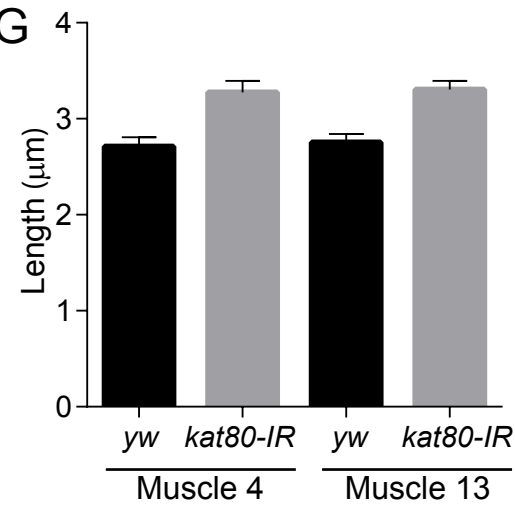
A

C380-Gal4, UAS-CD8-eGFP;;cha-Gal80

B

C380-Gal4, UAS-CD8-eGFP;;cha-Gal80 x Kat80-IR100 μ m

G



H

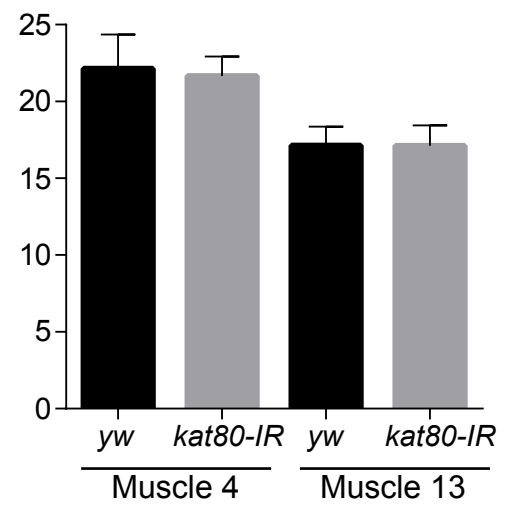


Figure S5
(Related to Figure 8)

Supplemental Data

Supplemental Figure S1. Electropherograms obtained via Sanger sequencing analysis of patient NG-PNH-226 and her parents. Whole-exome sequencing identified two compound heterozygous mutations in this patient (marked in red, wild-type (WT) marked in green). **(A)** The G>A transition at the splice acceptor site variant; **(B)** shows the G>A transition leading to the missense p.Gly578Asp variant. Co-segregation analysis revealed that the patient inherited the splice acceptor site variant from her mother and the missense variant from her father.

Supplemental Figure S2. Reduced protein levels in patient-derived dermal fibroblasts and possible aneuploidy upon expression of mutant forms of KATNB1: **(A)** Western analysis indicates reduced levels of KATNB1 in patient- as compared with parent-derived fibroblasts. **(B-C'')** HeLa cells transfected with WT and mutant forms of KATNB1. Reduced localization to the kinetochores and lagging chromosomes during metaphase (arrow) upon expression of mutant KATNB1.

Supplemental Figure S3. *kat80-IR* does not lead to increased apoptosis. TUNEL staining of *Drosophila* 3rd instar larval brains with *kat80-IR* clones does not show increased apoptosis within the clones.

Supplemental Figure S4. *kat80-IR* does not affect Notch or JAK/STAT signaling in the optic lobe. The GH146 driver was used to express *kat80-IR* in *Drosophila* larval brains. 3rd instar larval brains were stained for Notch and STAT. Images are 3D projections of equivalent Z stacks and were captured using identical confocal settings.

Supplemental Figure S5. *kat80-IR* does not affect muscle innervation. (A,B). Adult flies expressing *kat80-IR* under *C380-GAL4* driver, which directs expression in adult flight motoneurons (MN1-MN5), show normal innervation of the dorsal longitudinal flight muscle (DLM) via the PDMN nerve. **(C-F).**

Bouton size but not numbers were affected by *kat80-IR*: NMJ at muscle 4 **(C,D)** and muscle 13 **(E,F)** were imaged and quantified for size **(G)** and number **(H)**. Bouton size was significantly increased in *kat80-IR* 3rd instar larvae: muscle 4: mean± SEM: *yw*: 2.71±0.098; *kat80-IR*:3.276 ±0.118; *P* = 0.0023; muscle 13: mean± SEM: *yw*: 2.755±0.0853; *kat80-IR*:3.306 ±0.088; *P* = 0.0004

Supplemental Table S1A: Clinical Characteristics of patients with *KATNB1* mutations.

Supplemental Table S1B: Additional physical exam findings of patients.

Supplemental Table S1C: Radiological features of patients.

Supplemental Table S1D: Calculated relationships.

Supplemental Table S1E: Overlapping HBD segments between relatives.

Supplemental Table S1F: HBD segments of patients.

Supplemental Table S1G: *KATNB1* mutations identified by whole-exome sequencing.

Supplemental Table S1H: HBD variants of patients.

Experimental Procedures

Human subjects. The study protocol was approved by the Yale Human Investigation Committee (HIC) (protocol number 0908005592). Institutional review board approvals for genetic and MRI studies, along with written consent from all study subjects, were obtained by the referring physicians at the participating institutions. All fetal human tissues were collected under guidelines approved by the Yale HIC (protocol number 0605001466). Human fetal brains at 20 and 22 weeks of gestation were obtained from the Human Fetal Tissue Repository at the Albert Einstein College of Medicine (CCI number 1993-042).

Whole-exome capture and sequencing. NimbleGen 2.1M human exome array (Roche Nimblegen, Inc.) was used to capture the exomes of all samples according to the manufacturer's protocol with modifications, described previously^{1,2}. Sequencing of the library was performed on HiSeq2000 using a barcoding technology 74 base paired end, 6 samples per lane. The Illumina pipeline version 1.8 was used for image analysis and base calling.

Genome-wide genotyping. Selected samples were analyzed using 610K Quad Bead Chips according to the manufacturer's protocol (Illumina).

Sanger sequencing. Coding regions and exon-intron boundaries of *KATNB1* were evaluated by Sanger sequencing using standard protocols. Amplicons were cycle sequenced on ABI 9800 Fast Thermocyclers, and post cycle sequencing clean-up was carried out with CleanSEQ System (Beckman Coulter Genomics). The amplicons were analyzed on 3730xL DNA Analyzer (Applied Biosystems Inc.).

Identifying expression levels in the human fetal brain. The Human Brain Transcriptome database was used to identify the levels of *KATNB1* expression at selected time points throughout human development³. Procedure for interrogation and procurement of results were per their previously established protocols.

Exome sequence data analysis

Data preprocessing: Sequence reads were obtained through Illumina CASAVA pipeline. To achieve high quality alignment result, each read was subjected to trimming and filtering. We used cutadapt⁴ (v1.2.1) to trim PCR primer sequences from 3'-end. We also trimmed 3'-end of the read, starting from an ambiguous base call and continuing to trim systematically low quality 3'-end reads using an algorithm implemented in BWA⁵. We filtered reads if the resulting read length is shorter than 35 bp after

trimming. We also filtered reads with overall low quality (> 80% of the bases were < Q14) or low entropy/complexity (all but 3 or less bases are identical). A read pair was filtered if one of the ends was filtered. These trimming and filtering operations were carried out using an in-house perl script and the results were stored in FASTQ format files. We then aligned remaining sequence reads to a human genome reference (GRCh37) using a 1000 genomes project FASTA file (human_g1k_v37_decoy.fasta). Reads were initially aligned by BWA⁵ (v0.5.9-r16) and then unaligned reads and subset of the aligned reads were processed by Stampy⁶ (v1.0.21). Results were stored in BAM files. To exclude the contribution of PCR duplicates in the variant calling, we inferred duplicated DNA fragments and marked to be excluded from the downstream analysis using MarkDuplicates algorithm implemented in Picard-tools (<http://picard.sourceforge.net>).

Variant calling and filtering: We called variants for all 9 samples reported here together using freebayes (v9.9.2-36-gff98393) across the union of target and tiled intervals of two platforms (Agilent and Nimblegen) padded for 50 base pairs at each end. Variant (or allele) types detected were SNP, INDEL, MNP or other complex change (COMPLEX). We filtered the following SNPs: multi-allelic sites, QUAL < 20, QUAL / AO < 4, FS > 100, EPP > 300, or RPP > 200, where QUAL is the phred-scaled probability that the detected variant is false, AO is the depth of alternate-supporting allele, FS is the phred-scaled P-value of Fisher's exact test to detect strand bias in the reads, EPP and RPP are the end and read placement probability calculated by freebayes. For other variant types, the following variants were filtered: multi-allelic sites, QUAL < 10, QUAL / AO < 5, MQ < 20, MQM < 20, or ABP > 300, where MQ is the mean mapping quality, MQM is the mean mapping quality of alternate-supporting reads, ABP is the allele balance probability calculated by freebayes. To exclude low-confident genotype calls, we used the likelihood ratio between the maximum and the second highest phred-scaled genotype likelihoods, which we call GQ. We filtered heterozygous or homozygous genotypes if the GQ were less than 20 or 10, respectively

Variant annotation: We annotated functional consequence of the variants using variant effect predictor (v73). Using this information, we extracted variants that were located in exons or in splice regions up to 8 base pairs out from the exon-intron boundary. We annotated variants known to present in 1000 genomes project phase 1 (v3) and ESP6500SI (v2). Conservation scores inferred by GERP++ \ and phastCons \cite, repeat masked elements, and regions of known segmental duplications were also annotated. We used vcfintersect program of vcfliib to intersect our callset with known mutations in dbSNP (dbsnp_137.b37.excluding_sites_after_129.vcf) and a “gold-standard” INDEL sites (Mills_and_1000G_gold_standard.indels.b37.vcf).

Homozygosity by descent segment detection: To identify segments homozygous by descent (HBD), we used germline (v1-5-1). We included only sites without missing genotype calls as required by the program. We ran the program with the options “-err_hom 0 -err_het 0 -bits 32 -min_m 1 -homoz -homoz-only.” The identified segments were incorporated into the whole variant call set, and extended until we observed a heterozygous genotype. For relative pairs NG961 and LIS-711, we identified overlapping HBD segments and calculated the proportion of variant sites that coincide with each other. NG961 siblings shared 6 homozygous segments that were identical by descent, whereas only 1 of shared segments were IBD for LIS-711, consistent with the fact that LIS-711 patients were double first cousins.

Candidate mutations: To narrow down the candidate mutations, we filtered a mutation if one of the following conditions were met:

- (1) Any of the European American (EA) or African American (AA) cohorts of ESP6500SI had non-reference allele frequency > 0.005;
- (2) Any of EA or AA cohorts of ESP6500SI had one or more individuals with non-reference homozygous genotype;
- (3) Any of the 1000 genomes subpopulations had non-reference allele frequency > 0.005; or
- (4) It is a SNP for which the consequence is missense and both 2 programs (SIFT and PolyPhen) did not predict deleterious or damaging effect.

We searched for homozygous mutations shared by sibs (NG961 and LIS-711) within shared HBD segments.

Cell culture and Transfection

Skin Biopsy and Dermal Fibroblast Culture: A 4mm skin punch biopsies were taken under local anesthesia from the umbilical area of NG961-1, NG961-4, and their father (NG961-2) using a standard procedure^{7,8}. Samples were stored in Dulbecco’s Modified Eagle Medium (DMEM; Gibco, cat. no. 11965-084) supplemented with 10% heat-inactivated fetal bovine serum (FBS; Gibco, cat. no. 10438-026), 1% (1x) L-glutamine (Gibco, cat. no. 25030-081), 2% (1x) Penicillin-Streptomycin (Gibco, cat. No. 15140-122) and processed immediately on arrival. Following wash with PBS (Sigma Chemical Co., Saint Louis, USA), the samples were cut into small fragments, which were laid onto the surface of 100 mm² Petri dishes, in square areas marked by perpendicular lines made with scalpel blades. The fragments were allowed to air dry so as to adhere the dermis side of specimens to the culture dish. The fragments were then

cultured in DMEM with 10% heat-inactivated fetal bovine serum, 1% (1x) L-glutamine, 1% (1x) Penicillin-Streptomycin at 37°C. The fibroblasts typically grew within 7-9 days. HeLa cells were cultured in RPMI with 10% FCS and transfected using lipofectamine (Life technologies) and standard protocols.

Cloning and mutagenesis: Cloning of all genes in expression vectors was performed using the Gateway system (Life Sciences). Gateway BP and LR reactions were performed using BP and LR clonase, respectively, according to the vendor instructions. PCR reactions to amplify genes and/or gene fragments were performed using the high-fidelity Accuprime Pfx DNA polymerase (Life Sciences) while all mutagenesis reactions were performed using the high-fidelity Phusion DNA polymerase (New England Biolabs). Original full length cDNAs of various genes were purchased from the following vendors: KATNB1 from Openbiosystems/ Thermo Scientific (catalog MHS1011-58773); NDEL1 from Addgene (plasmid 12572); KATNA1 isoform 1 (catalog IHS1380-97652414; GenBank NM_007044) from Thermo Scientific; KATNA1 isoform 2 (catalog HsCD00510530) and PAFAH1/LIS1 (catalog HsCD00515632) from ASU (Arizona State University) DNA repository DNAs. B1/B2 PCR reactions were performed using primers below, in order to amplify the cDNA of all genes. For KATNA1, the B1 primer was combined with either one of the B2KATNA primers to amplify the two isoforms of KATNA1. B1/B2 PCR products containing the cDNA of the desired gene were purified using the PCR purification kit (Qiagen) and were recombined using BP clonase into the shuttle plasmid pDONR-zeo (Life Sciences). This yielded so-called cDNA ENTRY clones. All genes were fully sequenced at this stage. When needed, site-directed PCR mutagenesis was performed on these cDNAs ENTRY clone and each mutagenesis was followed by full sequencing of the respective cDNA to confirm the presence of the desired mutation and the absence of any novel PCR-caused mutation in the ORF of that gene. All mutagenesis primers were designed using the QuickChange Primer Design website (Agilent Technologies). Once the sequence of any ENTRY clone was confirmed, the respective plasmid DNA was recombined using LR clonase into a common, CMV promoter expression vector, pCDNA-DEST40 (Life Sciences), which carries a V5-HIS tandem tag at the 5' end of the Gateway cassette. All B2 primers depicted below have no STOP codon. This allowed tagging of all genes with the V5-HIS tandem tags present in pCDNA-DEST40.

For co-IP experiments, it was necessary to tag some of the genes with different peptide tags. Via a similar approach, we tagged LIS1, NDEL1 and KATNA1 with 6-Myc, Myc and HA in separate constructs. In addition, the commercially obtained cDNA of LIS1 had a missense mutation (A instead of G in position 982 which was repaired via PCR mutagenesis, using primers listed below).

The following KATNB1 mutations were targeted using site directed PCR mutagenesis: C>G P440R; C>T R459W; C>T S535L; G>A V45I; T>G L540R and G>A G578D. In each mutagenesis primer pair, the bold/underscored codon in the forward primer is the one targeted by mutagenesis. In each B1 primer, the bold/underscored GCCACC is the Kozak sequence, immediately in front of the start ATG codon. In each B2 primer, the bold/underscored codon is the last (non-STOP) codon of the ORF of the respective gene.

S535LF: GTGGCCATCAACGACCTGTTGGTGGTGGTG

S535LR: CACCACCACCAACAGGTCGTTGATGGCCAC

B1KATNB1: GGGGACAAGTTTGTACAAAAAAGCAGGCTTCGCCACCATGGCCACCCCTGTGGTCACCAAGAC

B2KATNB1ns: GGGGACCACTTTGTACAAGAAAGCTGGGTC CCAGTCCAGACTGGCCATGAGCAGGTGCA

B1NDEL: GGGGACAAGTTTGTACAAAAAAGCAGGCTTC GCCACC ATGGATGGTGAAGATATACCAGATT

B2NDELns: GGGGACCACTTTGTACAAGAAAGCTGGGTC CACACACACACTGAGAGGCAGCATAACC

B1-KATNA: GGGGACAAGTTTGTACAAAAAAGCAGGCTTC GCCACC ATGAGTCTTCTTATGATTAGTGA

B2KATNA1ns: GGGGACCACTTTGTACAAGAAAGCTGGGTC ATAGCATGATCCAAACTCAAATATCCA

B2KATNA2ns: GGGGACCACTTTGTACAAGAAAGCTGGGTC AGGACGCATCCCTGACGGCAAAGGAATATAGA

Antibodies and Immunostaining

For immunocytochemistry cells were fixed in 4% paraformaldehyde (4 % PFA) for 10 min or 4% PFA (10 min) followed by chilled methanol for 5 min at -20°C. Cells were pre-blocked in blocking solution containing 5% normal donkey serum (Jackson ImmunoResearch Laboratories,), 1% bovine serum albumin, 0.1% glycine, 0.1% lysine and 0.1% Triton X-100 in PBS for one hour at room temperature. After pre-blocking, sections were incubated in primary antibodies diluted in blocking solution on a horizontal shaker at 4°C for 2 hours, and washed in PBS at room temperature for three times. Sections were then incubated with secondary antibodies in blocking solution for 2 hours and washed in PBS for three times at room temperature. All samples slices were mounted with VECTASHIELD containing DAPI (Vector Laboratories), and imaged with Zeiss LSM or Leica TCS SP2 laser scanning confocal microscopy system. Primary antibodies used for immunocytochemistry are: anti-KATNB1 (Rabbit, 1:200; Sigma-Aldrich), Katanin A1 (R&D Systems, 1:100 dilution); NDEL1 (Origene, 1:50 dilution); V5 (Rockland Immuno); myc (Origene); HA (1:100 dilution); Dynein (Sigma, 1:100); Lis1 (Thermo-Fisher, 1:100). Alexa Fluor 488-

conjugated anti-rabbit IgG and Cy3 conjugated anti-mouse IgG raised in donkey (1:400; Life Technologies, NY) were used as secondary antibodies.

3rd instar wandering larvae were dissected in Schneider's medium (Sigma, St. Louis, MO), fixed in 100 mM Pipes (pH 6.9), 1 mM EGTA, and 1 mM MgCl₂ for 25 min and blocked for 1 h in 1X phosphate-buffered saline (PBS) containing 1% goat serum, 5% normal goat serum, 1% normal donkey serum and 0.3% Triton X-100 (PBT-Blocking). After blocking, specimens were extensively washed in PBT (PBS+0.3% Triton X-100) for 1 h and incubated with primary antibodies in PBT-Blocking overnight at 4°C. Primary antibodies were: rat anti-Miranda (1:100; Chris Doe); mouse anti- α tubulin (B512, Sigma, 1:1500); mouse anti- γ tubulin (GTU88, Sigma, 1:100); rabbit anti-Scrib, 1:1000 (Doe lab); anti-E-cadherin (DSHB); anti-Notch-intra (DSHB); anti-STAT92E (Steve Hou); rabbit anti-phospho-histone H3 (Upstate Biotechnology, Lake Placid, NY; 1:1000); katanin B1 (Sigma, 1:100). Primary antibodies were extensively rinsed off with PBS-BT for 1 h at room temperature, and specimens were incubated with fluorescently conjugated secondary antibodies (Life Technologies, NY) diluted in PBS-BT, followed by extensive rinsing with PBS-BT. For DNA labeling, specimens were mounted in Vectashield mounting medium with DAPI (Vector Labs). Brains were imaged using a Zeiss LSM 510 or Leica TCS SP2 laser scanning confocal microscope (Deerfield, IL) equipped with a 40X NA or 63X NA oil immersion objective, respectively. Figures were assembled in Adobe Photoshop (San Jose, CA). 3D projections and quantifications were performed using IMARIS.

Immunoprecipitation

HeLa cells were transfected with either V5 tagged WT or mutant forms of KATNB1 along with 6XMyc-KATNA1 or HA-NDEL1 using Lipofectamine (Life Technologies, NY). 48 hours after transfection, cells were lysed using a triton-X100 based buffer containing protease inhibitor cocktail (Calbiochem). Clarified supernatants were used for immunoprecipitation using Dynabeads (Life Technologies) according to the Suppliers protocol. Immunoprecipitates were analyzed by Western analysis using standard protocols. The samples were run on 10% SDS-PAGE gels (BioRad) and Western blots were performed according to standard methods. In brief, lysates were separated on gradient gels (4-16%, BioRad) SDS-PAGE gels and transferred to nitrocellulose membranes. After blocking with 5% milk, the membranes were incubated first with rabbit anti-tag antibodies and then with a secondary HRP-conjugated anti-rabbit IgG (Jackson ImmunoResearch Labs). Signals were detected with chemiluminescence reagent (Biorad).

Fly Genetics

Oregon R or *yw* flies were used as wild-type controls. Other fly strains used include: *w;warniu-GAL4, UAS-Miranda::GFP, UAS-Zeus::mCHERRY/ Cyo;Dr/TM6b* (Chris Doe); *w,UAS-CD8-GFP;D42-gal4,chagal80;c380-Gal4, UAS-CD8-GFP;;cha-gal80; hsFLP;Act-FRT-CD2-FRTgal4,UAS-CD8(n); y[1] w[1118]; P{w[+m*]=GawB}GH146* (Bloomington Stock Center); *kat80* RNAi lines were obtained from VDRC. Three independent *kat80* RNAi lines showed similar results.

Time-lapse Analysis of Neuroblast Cell Division in Larval Brain Explants

Wandering 3rd instar larvae of *warniu-Gal4* crossed to either *yw* or *kat80-IR* flies were dissected in Schneider's insect medium (Life Technologies) supplemented with 7.5% fetal bovine serum (FBS). Four to five larval brains were immediately transferred into 200 μ l of Schneider's medium supplemented with 7.5% FBS, 0.5 mM ascorbic acid, and fatbodies obtained from 10 wild-type wandering 3rd instar larvae. Brains were mounted with fatbody tissue on a standard membrane (Yellow Springs Instruments, Yellow Springs, OH) and placed on a stainless steel slide as previously described⁹. Brains were imaged using a Zeiss laser scanning confocal microscope equipped with a 63X NA oil immersion objective. For the mitotic analysis of neuroblasts, stacks containing four focal planes spaced by 1.5 μ m were acquired at intervals of 1 minute 30 seconds. Time-lapse image series were converted into movies using IMARIS. All movie frames are maximum intensity projections.

Neuron visualization and dendritic analysis

For visualization of larval sensory cells and to study the effect of *kat80* loss, *UAS-CD8-GFP* or *UAS-CD-GFP, kat80-IR* were expressed under the control of the *ppk-GAL4* driver that expresses strongly in all class IV sensory neurons and weakly in class III neurons^{10,11}. Analysis was focused on class IV dendrites, which are morphologically distinguishable from class III branches¹⁰. Morphological analysis of dendrites was exclusively restricted to the dorsally located *ddaC* neuron in segments A3 and A4¹⁰. Images were taken using a Bio-rad 1024 confocal microscope. The total number of terminal dendrites was counted manually on z-projections using the cell count function of ImageJ software. Quantification of dendritic coverage was performed in ImageJ software by individually overlaying a grid of squares of 0.1% of the total pixel size of each z-projection image and calculating the number of boxes containing dendrites as a percentage of total box number within the dendritic field.

For visualization of dendrites of adult flight motoneurons and to study the effect of *kat80* loss, *UAS-CD8-GFP* or *UAS-CD-GFP, kat80-IR* were expressed under the control of the *D42-GAL4* or *C380-GAL4* driver that drive expression mainly in motoneurons^{12,13}. Additionally, *GAL80* was expressed under the choline-

acetyl transferase promoter (*Cha-GAL80*) to suppress GAL4 activity in all cholinergic neurons¹⁴ some of which are presynaptic partners of the flight motoneurons^{13,15}. Mouse anti-GFP primary antibody (Rockland Immunochemicals) with fluorescently conjugated secondary antibodies were used as described previously^{16,17} for better visualization of GFP labeled dendrites.

To visualize NMJ arbors third-instar larvae were dissected and fixed as described¹⁸. To visualize NMJ arbors, anti-HRP immunocytochemistry was performed as described¹⁹ with 0.05% diaminobenzidine (DAB; Polysciences, Inc., Warrington, PA) in the presence of 0.003% H₂O₂. Larval fillets were mounted in glycerol and examined using bright field imaging. All data were taken from muscles in segment A3 and restricted to type Ib boutons.

Behavioral experiments

Dendritic defects after targeted manipulation of adult flight motoneurons was performed as previously described¹⁷. The flight assay was performed according to the method of Drummond et al.^{20,21} and as modified by Nelson et al.

Mouse experiments:

In situ hybridization: Embryonic and postnatal brains were fixed, respectively, by immersion in or intracardial perfusion with 4% paraformaldehyde (PFA), post-fixed in 30% sucrose in 4% PFA and sectioned on a cryomicrotome (Leica Microsystems, Wetzlar, Germany). Sections were processed for *in situ* hybridization as described previously²². RNA probes complementary to mouse *katanin b1* (bases 105 to 908 of the mouse *katanin b1* cDNA) were labeled with digoxigenin-11-UTP. Sections were analyzed using a Stemi stereomicroscope or Axiomager (Zeiss, Oberkochen, Germany) fitted with an AxioCam MRc5 digital camera. Images were captured using AxioVision software (Zeiss) and assembled in Adobe Photoshop.

Zebrafish studies:

***Katnb1* expression pattern analysis by whole-mount *in situ* hybridization:** Whole-mount *in situ* hybridization was performed as described²³. DNA template for anti-sense *katnb1* (accession number: NM_213018) riboprobe was synthesized by PCR amplification from 24 hpf (hours post fertilization)

zebrafish cDNA with the following primer set: 5'-TGGTGGACGTCCTCAACATA-3' and 5'-AGTCCAGAGGGGCCATAAGT-3'.

katnb1 morpholino injection and image analysis: 9 ng of katnb1 morpholino was injected into 1-cell stage wild type embryos as described²³. Dorsal view images of 72 hpf control and morphant embryos were taken by a Leica M205 FA dissecting microscope with LAS AF software. Brain size was subsequently measured in ImageJ. Statistical analysis was carried out in Microsoft Excel. katnb1 ATG morpholino: 5'-TTGTGTGGACTGGGTCAAATCACTC-3' (Genetools).

References:

1. Bilguvar, K. *et al.* Whole-exome sequencing identifies recessive WDR62 mutations in severe brain malformations. *Nature* **467**, 207-10 (2010).
2. Choi, M. *et al.* Genetic diagnosis by whole exome capture and massively parallel DNA sequencing. *Proc Natl Acad Sci U S A* **106**, 19096-101 (2009).
3. Kang, H.J. *et al.* Spatio-temporal transcriptome of the human brain. *Nature* **478**, 483-9 (2011).
4. Martin, M. Cutadapt removes adapter sequences from high-throughput sequencing reads. *2011* **17**(2011).
5. Li, H. *et al.* The Sequence Alignment/Map format and SAMtools. *Bioinformatics* **25**, 2078-2079 (2009).
6. Lunter, G. & Goodson, M. Stampy: a statistical algorithm for sensitive and fast mapping of Illumina sequence reads. *Genome Res* **21**, 936-9 (2011).
7. Levitt, J., Bernardo, S. & Whang, T. Videos in clinical medicine. How to perform a punch biopsy of the skin. *N Engl J Med* **369**, e13 (2013).
8. Zuber, T.J. Punch biopsy of the skin. *Am Fam Physician* **65**, 1155-8, 1161-2, 1164 (2002).
9. Kiehart, D.P., Montague, R.A., Rickoll, W.L., Foard, D. & Thomas, G.H. High-resolution microscopic methods for the analysis of cellular movements in *Drosophila* embryos. *Methods Cell Biol* **44**, 507-32 (1994).
10. Grueber, W.B., Jan, L.Y. & Jan, Y.N. Tiling of the *Drosophila* epidermis by multidendritic sensory neurons. *Development* **129**, 2867-78 (2002).
11. Grueber, W.B. *et al.* Projections of *Drosophila* multidendritic neurons in the central nervous system: links with peripheral dendrite morphology. *Development* **134**, 55-64 (2007).
12. Budnik, V. Synapse maturation and structural plasticity at *Drosophila* neuromuscular junctions. *Curr Opin Neurobiol* **6**, 858-67 (1996).
13. Vonhoff, F., Kuehn, C., Blumenstock, S., Sanyal, S. & Duch, C. Temporal coherency between receptor expression, neural activity and AP-1-dependent transcription regulates *Drosophila* motoneuron dendrite development. *Development* **140**, 606-16 (2013).
14. Aberle, H. *et al.* wishful thinking encodes a BMP type II receptor that regulates synaptic growth in *Drosophila*. *Neuron* **33**, 545-58 (2002).
15. Duch, C., Vonhoff, F. & Ryglewski, S. Dendrite elongation and dendritic branching are affected separately by different forms of intrinsic motoneuron excitability. *J Neurophysiol* **100**, 2525-36 (2008).
16. Vonhoff, F. & Duch, C. Tiling among stereotyped dendritic branches in an identified *Drosophila* motoneuron. *J Comp Neurol* **518**, 2169-85 (2010).
17. Vonhoff, F., Williams, A., Ryglewski, S. & Duch, C. *Drosophila* as a model for MECP2 gain of function in neurons. *PLoS One* **7**, e31835 (2012).

18. Lnenicka, G.A. & Keshishian, H. Identified motor terminals in *Drosophila* larvae show distinct differences in morphology and physiology. *J Neurobiol* **43**, 186-97 (2000).
19. Johansen, J., Halpern, M.E., Johansen, K.M. & Keshishian, H. Stereotypic morphology of glutamatergic synapses on identified muscle cells of *Drosophila* larvae. *J Neurosci* **9**, 710-25 (1989).
20. Drummond, D.R., Hennessey, E.S. & Sparrow, J.C. Characterisation of missense mutations in the Act88F gene of *Drosophila melanogaster*. *Mol Gen Genet* **226**, 70-80 (1991).
21. Nelson, H.B. *et al.* Calmodulin point mutations affect *Drosophila* development and behavior. *Genetics* **147**, 1783-98 (1997).
22. Tanriover, G. *et al.* PDCD10, the gene mutated in cerebral cavernous malformation 3, is expressed in the neurovascular unit. *Neurosurgery* **62**, 930-8; discussion 938 (2008).
23. Hegarty, J.M., Yang, H. & Chi, N.C. UBIAD1-mediated vitamin K2 synthesis is required for vascular endothelial cell survival and development. *Development* **140**, 1713-9 (2013).